J. Fluid Mech. (2013), *vol.* 726, *pp.* 62–99.
doi:10.1017/jfm.2013.215

Dynamic modelling of sea-surface roughness for large-eddy simulation of wind over ocean wavefield

Di Yang[1], Charles Meneveau[1,2] and Lian Shen[3,4],†

[1]Department of Mechanical Engineering, Johns Hopkins University, Baltimore, MD 21218, USA

[2]Center for Environmental and Applied Fluid Mechanics, Johns Hopkins University, Baltimore, MD 21218, USA

[3]Department of Mechanical Engineering, University of Minnesota, Minneapolis, MN 55455, USA

[4]St Anthony Falls Laboratory, University of Minnesota, Minneapolis, MN 55414, USA

(Received 31 May 2012; revised 9 January 2013; accepted 22 April 2013;
first published online 30 May 2013)

Wind blowing over the ocean surface can be treated as a turbulent boundary layer over a multiscale rough surface with moving roughness elements, the waves. Large-eddy simulation (LES) of such flows is challenging because LES resolves wind–wave interactions only down to the grid scale, Δ, while the effects of subgrid-scale (SGS) waves on the wind need to be modelled. Usually, a surface-layer model based on the law of the wall is used; but the surface roughness has been known to depend on the local wind and wave conditions and is difficult to parameterize. In this study, a dynamic model for the SGS sea-surface roughness is developed, with the roughness corresponding to the SGS waves expressed as $\alpha_w \sigma_\eta^\Delta$. Here, σ_η^Δ is the effective amplitude of the SGS waves, modelled as a weighted integral of the SGS wave spectrum based on the geometric and kinematic properties of the waves for which five candidate expressions are examined. Moreover, α_w is an unknown dimensionless model coefficient determined dynamically based on the first-principles constraint that the total surface drag force or average surface stress must be independent of the LES filter scale Δ. The feasibility and consistency of the dynamic sea-surface roughness models are assessed by *a priori* tests using data from high-resolution LES with near-surface resolution, appropriately filtered. Also, these data are used for *a posteriori* tests of the dynamic sea-surface roughness models in LES with near-surface modelling. It is found that the dynamic modelling approach can successfully capture the effects of SGS waves on the wind turbulence without *ad hoc* prescription of the model parameter α_w. Also, for σ_η^Δ, a model based on the kinematics of wind–wave relative motion achieves the best performance among the five candidate models.

Key words: turbulence modelling, turbulent boundary layers, wind–wave interactions

1. Introduction

The physics of wind-waves and the interactions between wind turbulence and ocean waves play essential roles in many important geophysical phenomena and engineering

† Email address for correspondence: shen@umn.edu

applications. They determine the exchange of mass, momentum and heat between the atmosphere and the oceans, crucial for shaping our understanding and prediction of weather and global climate. Wave and wind loads are vital to the safety and operation of surface ships and offshore structures. Knowledge of wind and wave fields forms the basis for the design and operation of offshore wind farms and wave energy converters. The wind-wave kinematics also have significant influence on the transport of pollutants such as oil slicks at sea surfaces.

The flow-over-wave-surface problem has been an active research topic. Many theoretical studies (Phillips 1957; Miles 1957, 1993; Janssen 1991; Belcher & Hunt 1993, among others) have focused on explaining the mechanism of wind–wave generation and growth. Meanwhile, the quantification of wind–wave energy and momentum transfer and wavefield evolution has relied substantially on field and laboratory measurements (Dobson 1971; Elliott 1972; Snyder *et al.* 1981; Hristov, Miller & Friehe 2003; Donelan *et al.* 2006; Peirson & Garcia 2008, among many others).

In addition to theoretical and experimental studies, numerical simulations of wind turbulence over waves have contributed substantially to our understanding. Early studies focused on the Reynolds-averaged Navier–Stokes (RANS) equations (e.g. Townsend 1972; Gent & Taylor 1976; Al-Zanaidi & Hui 1984; van Duin & Janssen 1992; Mastenbroek *et al.* 1996), yielding many interesting and valuable findings. However, the results were found to be quite sensitive to the choice of turbulence closure for the Reynolds stresses (see, e.g., van Duin & Janssen 1992; Mastenbroek *et al.* 1996). In recent years, the growth of computing power has made direct numerical simulation (DNS) feasible for the study of wind turbulence over waves, under idealized conditions. Through DNS, the fine details of turbulent flows in the vicinity of the wave surface can be resolved (e.g. Sullivan, McWilliams & Moeng 2000; Kihara *et al.* 2007; Yang & Shen 2009, 2010). However, the high computational cost of DNS limits its application to relatively low Reynolds numbers. As a result, DNS is used mainly as a research tool for studies of simplified, canonical problems.

Large-eddy simulation (LES) has been widely used in the study of atmospheric boundary layer flows (e.g. Deardorff 1973; Moeng 1984; Albertson & Parlange 1999; Porté-Agel, Meneveau & Parlange 2000; Kumar *et al.* 2010). The LES resolves the grid-scale (GS) motions explicitly, with the subgrid-scale (SGS) effect modelled. Because only the small-scale motions need to be modelled while the motions at other scales are simulated directly, LES has become a promising approach for the study of wind turbulence over ocean waves (Sullivan *et al.* 2008; Liu *et al.* 2010; Sullivan, McWilliams & Hristov 2010).

One important open issue for LES of wind over waves, which is the subject of the present study, is the representation of wave surface features that fall below the grid resolution in the LES, i.e. modelling of SGS roughness effects. While at scales larger than short gravity waves the wind field can be treated as a turbulent boundary layer over a wavy and rough surface (Donelan 1990; Janssen 1991), fully resolving the near-surface region is prohibitively expensive and a surface-layer model is needed (see the review by Piomelli & Balaras (2002)). LES with near-surface modelling (LESns-M) is required, which in the engineering literature is denoted as LES with near-wall modelling (LES-NWM; see, e.g., Pope 2000), including specification of the surface roughness scale. However, unlike the static rough wall applications most often considered in the literature on turbulence over rough surfaces, the roughness elements at sea (i.e. different wave components) are all in motion. Moreover, elements

of different sizes move at different speeds according to the wave-dispersion relation, posing a challenge to modelling of sea-surface roughness.

Previous studies showed that short gravity waves are primarily responsible for the sea-surface roughness (see, e.g., Caudal 1993; Makin, Kudryavtsev & Mastenbroek 1995). In the literature, the sea-surface roughness scale z_0 is often parameterized as (e.g. Smith 1988; Fairall *et al.* 1996)

$$z_0 = z_{0,s} + z_{0,w}. \tag{1.1}$$

Here, $z_{0,s} = 0.11\nu_a/u_*$ is the roughness for a smooth surface, with ν_a being the kinematic viscosity of air and u_* being the friction velocity of wind; and $z_{0,w}$ is the roughness corresponding to short surface waves. The short waves are often assumed to be in equilibrium with the local wind, so that $z_{0,w}$ is parameterized by the Charnock relationship (Charnock 1955)

$$z_{0,w} = \alpha_{ch}\frac{u_*^2}{g}, \tag{1.2}$$

where the Charnock constant α_{ch} is an empirical coefficient and g is the gravitational acceleration. The value of α_{ch} has been evaluated based on field data (e.g. Fairall *et al.* 1996; Johnson *et al.* 1998). However, instead of being a constant, α_{ch} was found to depend on the wave condition. As a result, the parameterization of sea-surface roughness displays significant variations among different studies (see, e.g., the reviews of Donelan (1990) and Toba, Smith & Ebuchi (2001)). In the literature, sea-state scaling (e.g. Taylor & Yelland 2001) and wave-age scaling (e.g. Smith *et al.* 1992) have been used, based, respectively, on the following expressions:

$$\frac{z_{0,w}}{\eta_{rms}} = A_1\left(\frac{\eta_{rms}}{\lambda_p}\right)^{B_1}, \quad \frac{z_{0,w}}{\eta_{rms}} = A_2\left(\frac{V}{c_p}\right)^{B_2}. \tag{1.3}$$

Here, η_{rms} is the root-mean-square (r.m.s.) of the surface elevation η; λ_p and c_p are, respectively, the wavelength and wave phase speed at the wave spectrum peak; V is a reference wind velocity, which can be the wind friction velocity u_*, the mean wind speed at 10 m above the sea surface U_{10}, or the mean wind speed at the elevation of $\lambda_p/2$ above the sea surface $U_{\lambda_p/2}$. The coefficients A_1, B_1, A_2 and B_2 are determined by fitting field measurement data (e.g. Donelan 1990). Previous studies have shown that these parameterizations may work well for some sea conditions, but not in others. Thus, no universally consistent parameterization has been found yet (Drennan, Taylor & Yelland 2005). As a result, so far in LES of wind over waves, only the simplest treatment, in which z_0 was assigned a constant value of 2×10^{-4} m, has been applied (e.g. Sullivan *et al.* 2008, 2010), which is unable to address dependencies on wave dynamics.

Recently, Anderson & Meneveau (2011) have developed a dynamic method for the modelling of surface roughness of wind turbulence over land, consisting of a multiscale (static) terrain. Fundamental to the dynamic model is the decomposition of the total surface stress into a resolved and an SGS part. The dynamic method uses the fundamental constraint that the total stress must be invariant with respect to the filter scale. The unknown coefficient in the model is thus determined using a GS filter and a test filter. In traditional LESns-M, such coefficients must be prescribed *ad hoc*. The proposed dynamic approach has the advantage of determining the model coefficient during the simulation without *ad hoc* prescriptions and assumptions. To date, it has been successfully applied to atmospheric boundary-layer flows over rough multiscale

land surfaces with power-law surface spectra (Anderson & Meneveau 2011), as well as over fluvial-like landscapes (Anderson *et al.* 2012).

In the present study, we extend the dynamic modelling of SGS surface roughness from static land surfaces to moving water surface waves. As in Anderson & Meneveau (2011), the roughness length is expressed as the product of two factors: an effective amplitude of the SGS waves, which unlike the static case of Anderson & Meneveau (2011) now contains both the geometric information of the SGS wave surface elevation as well as the kinematic properties of the waves; and an unknown dimensionless model coefficient, which is determined dynamically using the resolved flow information and the constraint that the total surface force or average surface stress is invariant with respect to the filter scale in LES. Several alternate models for the effective amplitude of the SGS waves are developed and tested.

In our simulation, the flow solver for wind over a broadband wavefield developed by Yang & Shen (2011*b*) is employed, with the original DNS turbulence solver upgraded to LES by including SGS stress and SGS surface-layer models. The sea-surface wavefield is simulated as a potential flow using a high-order spectral method (HOSM) (Dommermuth & Yue 1987). High-resolution LES with near-surface (or near-wall, Pope 2000) resolution, to be denoted henceforth as LESns-R, is performed for a variety of wind and wave conditions to obtain a database as a benchmark for the evaluation of sea-surface roughness models. The result of LESns-R is validated by comparisons with experimental, theoretical and numerical results in the literature. *A priori* and *a posteriori* tests are performed to evaluate the performance of several candidate sea-surface roughness models. In particular, *a posteriori* tests use LESns-M with the new dynamic sea-surface roughness models implemented.

This paper is organized as follows. The numerical methods for wind and wave simulations are introduced in § 2. The dynamic models of SGS sea-surface roughness are presented in § 3. The data of LESns-R and the results of the *a priori* and *a posteriori* tests of the dynamic sea-surface roughness models are discussed in § 4. Finally, concluding remarks are provided in § 5.

2. Numerical method for wind and wave simulations

2.1. *LES of wind turbulence*

In this study, we consider three-dimensional turbulent flows over water waves. The coordinate system is denoted as $x_i(i = 1, 2, 3) = (x, y, z)$, where x and y are the horizontal coordinates and z is the vertical coordinate, with $z = 0$ being the mean water level and $u_i(i = 1, 2, 3) = (u, v, w)$ are the velocity components in the x, y and z directions, respectively.

The motion of wind turbulence is described by the filtered Navier–Stokes equations

$$\frac{\partial \widetilde{u}_i}{\partial t} + \widetilde{u}_j \frac{\partial \widetilde{u}_i}{\partial x_j} = -\frac{1}{\rho_a}\frac{\partial \widetilde{p}}{\partial x_i} - \frac{\partial \tau_{ij}^d}{\partial x_j} + \nu_a \frac{\partial^2 \widetilde{u}_i}{\partial x_j \partial x_j} - \frac{1}{\rho_a}\Pi \delta_{i1}, \tag{2.1}$$

$$\frac{\partial \widetilde{u}_i}{\partial x_i} = 0. \tag{2.2}$$

Here, $(\widetilde{\ldots})$ indicates filtering at the grid scale, Δ, in LES; $\tau_{ij} = \widetilde{u_i u_j} - \widetilde{u}_i \widetilde{u}_j$ is the SGS stress tensor, and τ_{ij}^d is its trace-free part; $\widetilde{p}$ is the actual pressure of air (strictly speaking the modified pressure, since it includes the trace of the SGS stress tensor); and Π is the streamwise pressure gradient imposed to drive the flow in the simulations.

For a statistically steady and fully developed flow,

$$\Pi = -\frac{\rho_a u_*^2}{\overline{H}}, \tag{2.3}$$

where $\overline{H}$ is the mean height of the computational domain.

The simulation domain is bounded by a free-slip boundary at the top and a waving boundary at the bottom. The lateral boundaries are treated as periodic. A boundary-fitted grid system is used above the wave surface, as illustrated in figure 1. The irregular wave surface-bounded domain in the physical space (x, y, z, t) is transformed to a right rectangular prism in the computational space (ξ, ψ, ζ, τ) with the following algebraic mapping:

$$\tau = t, \quad \xi = x, \quad \psi = y, \quad \zeta = \frac{z - \widetilde{\eta}}{\widetilde{H}(x, y, t)} = \frac{z - \widetilde{\eta}(x, y, t)}{\overline{H} - \widetilde{\eta}(x, y, t)}. \tag{2.4}$$

Here, the height of the physical domain, $\widetilde{H}(x, y, t)$, is decomposed into the average height $\overline{H}$ and a wave-induced variation $-\widetilde{\eta}(x, y, t)$.

Applying the algebraic mapping to (2.1) and (2.2) gives the following governing equations in the computational space:

$$\begin{aligned}
&\frac{\partial \widetilde{u}}{\partial \tau} + \zeta_t \frac{\partial \widetilde{u}}{\partial \zeta} + \widetilde{u}\left(\frac{\partial \widetilde{u}}{\partial \xi} + \zeta_x \frac{\partial \widetilde{u}}{\partial \zeta}\right) + \widetilde{v}\left(\frac{\partial \widetilde{u}}{\partial \psi} + \zeta_y \frac{\partial \widetilde{u}}{\partial \zeta}\right) + \widetilde{w}\zeta_z \frac{\partial \widetilde{u}}{\partial \zeta} \\
&\quad = -\frac{1}{\rho_a}\left(\frac{\partial \widetilde{p}}{\partial \xi} + \zeta_x \frac{\partial \widetilde{p}}{\partial \zeta}\right) - \frac{\partial \tau_{11}^d}{\partial \xi} - \zeta_x \frac{\partial \tau_{11}^d}{\partial \zeta} - \frac{\partial \tau_{12}^d}{\partial \psi} - \zeta_y \frac{\partial \tau_{12}^d}{\partial \zeta} - \zeta_z \frac{\partial \tau_{13}^d}{\partial \zeta} \\
&\qquad + \nu_a \nabla^2 \widetilde{u} - \frac{1}{\rho_a}\Pi,
\end{aligned} \tag{2.5}$$

$$\begin{aligned}
&\frac{\partial \widetilde{v}}{\partial \tau} + \zeta_t \frac{\partial \widetilde{v}}{\partial \zeta} + \widetilde{u}\left(\frac{\partial \widetilde{v}}{\partial \xi} + \zeta_x \frac{\partial \widetilde{v}}{\partial \zeta}\right) + \widetilde{v}\left(\frac{\partial \widetilde{v}}{\partial \psi} + \zeta_y \frac{\partial \widetilde{v}}{\partial \zeta}\right) + \widetilde{w}\zeta_z \frac{\partial \widetilde{v}}{\partial \zeta} \\
&\quad = -\frac{1}{\rho_a}\left(\frac{\partial \widetilde{p}}{\partial \psi} + \zeta_y \frac{\partial \widetilde{p}}{\partial \zeta}\right) - \frac{\partial \tau_{21}^d}{\partial \xi} - \zeta_x \frac{\partial \tau_{21}^d}{\partial \zeta} - \frac{\partial \tau_{22}^d}{\partial \psi} - \zeta_y \frac{\partial \tau_{22}^d}{\partial \zeta} - \zeta_z \frac{\partial \tau_{23}^d}{\partial \zeta} + \nu_a \nabla^2 \widetilde{v},
\end{aligned} \tag{2.6}$$

$$\begin{aligned}
&\frac{\partial \widetilde{w}}{\partial \tau} + \zeta_t \frac{\partial \widetilde{w}}{\partial \zeta} + \widetilde{u}\left(\frac{\partial \widetilde{w}}{\partial \xi} + \zeta_x \frac{\partial \widetilde{w}}{\partial \zeta}\right) + \widetilde{v}\left(\frac{\partial \widetilde{w}}{\partial \psi} + \zeta_y \frac{\partial \widetilde{w}}{\partial \zeta}\right) + \widetilde{w}\zeta_z \frac{\partial \widetilde{w}}{\partial \zeta} \\
&\quad = -\frac{1}{\rho_a}\left(\zeta_z \frac{\partial \widetilde{p}}{\partial \zeta}\right) - \frac{\partial \tau_{31}^d}{\partial \xi} - \zeta_x \frac{\partial \tau_{31}^d}{\partial \zeta} - \frac{\partial \tau_{32}^d}{\partial \psi} - \zeta_y \frac{\partial \tau_{32}^d}{\partial \zeta} - \zeta_z \frac{\partial \tau_{33}^d}{\partial \zeta} + \nu_a \nabla^2 \widetilde{w},
\end{aligned} \tag{2.7}$$

$$\frac{\partial \widetilde{u}}{\partial \xi} + \zeta_x \frac{\partial \widetilde{u}}{\partial \zeta} + \frac{\partial \widetilde{v}}{\partial \psi} + \zeta_y \frac{\partial \widetilde{v}}{\partial \zeta} + \zeta_z \frac{\partial \widetilde{w}}{\partial \zeta} = 0, \tag{2.8}$$

where

$$\begin{aligned}
\nabla^2 = &\frac{\partial^2}{\partial \xi^2} + \frac{\partial^2}{\partial \psi^2} + 2\zeta_x \frac{\partial^2}{\partial \xi \partial \zeta} + 2\zeta_y \frac{\partial^2}{\partial \psi \partial \zeta} + (\zeta_x^2 + \zeta_y^2 + \zeta_z^2)\frac{\partial^2}{\partial \zeta^2} \\
&+ (\zeta_{xx} + \zeta_{yy})\frac{\partial}{\partial \zeta}.
\end{aligned} \tag{2.9}$$

Here, the subscripts 't', 'x' and 'y' for ζ denote the partial derivatives of ζ with respect to t, x and y, respectively.

For spatial discretization, we use a Fourier-series-based pseudo-spectral method on an evenly spaced collocated grid in the horizontal directions, and a second-order finite-difference method on a staggered grid in the vertical direction. In LESns-R, the vertical grid is clustered near the wave surface to have high resolution in the

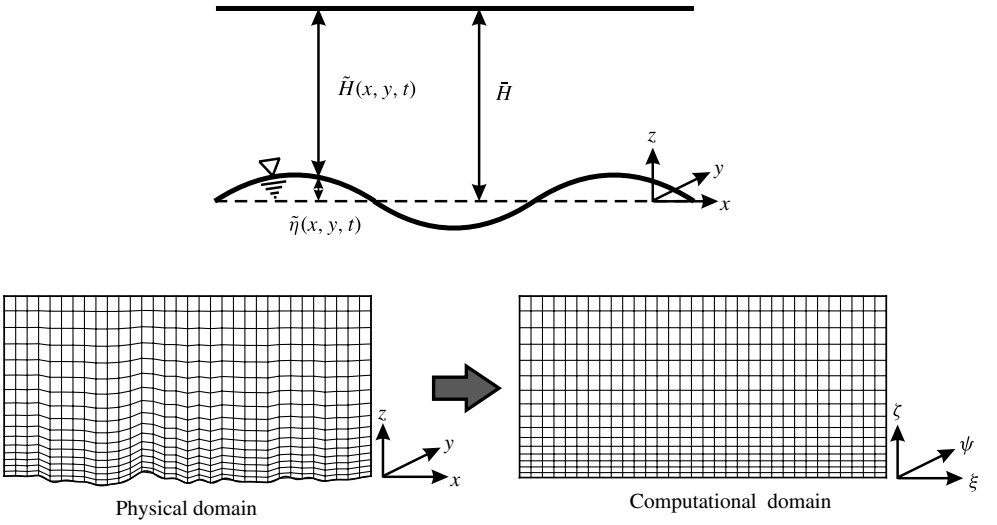

FIGURE 1. Illustration of coordinate transformation. The irregular wave surface-bounded domain in the physical space (x, y, z, t) is transformed into a right rectangular prism in the computational space (ξ, ψ, ζ, τ). Only a vertical cross-section in the three-dimensional space is plotted here.

near-surface region of the boundary layer. In LESns-M, the vertical grid is evenly spaced; the near-surface region is not well resolved, relying on a surface-layer model instead to provide the surface stress to the wind field. Details of the surface-layer model are given in § 3. In the momentum equation, the SGS stress tensor is modelled using the dynamic Smagorinsky model (Germano *et al.* 1991; Lilly 1992) including planar, surface parallel, averaging in the computational domain. For the grid- and test-filtering operators in the governing equation, we use a two-dimensional spectral cutoff filter in the (ξ, ψ)-plane in the computational space. For surface-resolving LES, this approach is appropriate. For LESns-M, it was shown in Porté-Agel *et al.* (2000) that a scale-dependent dynamic approach provides more accurate predictions of turbulence in the near-surface region. However, in order to avoid increased modelling complexity, and to avoid switching between SGS models for representing the turbulent bulk flow, in this study we opt to use the standard dynamic Smagorinsky model.

The governing equations are integrated in time with a fractional-step method. First, the momentum equations without the pressure terms are advanced in time with a second-order Adams–Bashforth scheme. In order to enforce the incompressibility constraint, a pressure Poisson equation is then solved to provide a correction to the velocity field. Details and validations of the numerical method are provided by Yang & Shen (2011*a*).

2.2. *HOSM for the simulation of sea-surface waves*

The motions of the sea-surface waves are simulated using a potential-flow-based HOSM (Dommermuth & Yue 1987; see also West, Brueckner & Janda 1987). The HOSM simulates nonlinear waves using the Zakharov formulation (Zakharov 1968), in which the wave motion is described by the surface elevation η and the surface potential Φ^s. Here, $\Phi^s = \Phi(x, y, z = \eta(x, y, t), t)$ with Φ being the velocity potential.

Starting from the kinematic and dynamic free-surface boundary conditions (e.g. Mei, Stiassnie & Yue 2005), three steps are taken (Dommermuth & Yue 1987): (i) use a perturbation series of Φ with respect to wave steepness to order M,

$$\Phi(x, y, z, t) = \sum_{m=1}^{M} \Phi^{(m)}(x, y, z, t); \tag{2.10}$$

(ii) express Φ^s using Taylor series expansion about $z = 0$ to the order corresponding to (i),

$$\Phi^s(x, y, t) = \sum_{m=1}^{M} \sum_{\ell=0}^{M-m} \frac{\eta^\ell}{\ell!} \frac{\partial^\ell}{\partial z^\ell} \Phi^{(m)}(x, y, z, t)\bigg|_{z=0}; \tag{2.11}$$

and (iii) represent $\Phi^{(m)}$ using an eigenfunction expansion with N modes,

$$\Phi^{(m)}(x, y, z, t) = \sum_{n=1}^{N} \Phi_n^{(m)}(t) \Psi_n(x, y, z). \tag{2.12}$$

The evolution equations for η and Φ^s are obtained as (Dommermuth & Yue 1987)

$$\frac{\partial \eta}{\partial t} = -\nabla_h \eta \cdot \nabla_h \Phi^s + (1 + \nabla_h \eta \cdot \nabla_h \eta) \times \left[\sum_{m=1}^{M} \sum_{\ell=0}^{M-m} \frac{\eta^\ell}{\ell!} \sum_{n=1}^{N} \Phi_n^{(m)}(t) \frac{\partial^{\ell+1} \Psi_n(x, y, z)}{\partial z^{\ell+1}}\bigg|_{z=0} \right], \tag{2.13}$$

$$\frac{\partial \Phi^s}{\partial t} = -g\eta - \frac{1}{2} \nabla_h \Phi^s \cdot \nabla_h \Phi^s + \frac{1}{2} (1 + \nabla_h \eta \cdot \nabla_h \eta) \times \left[\sum_{m=1}^{M} \sum_{\ell=0}^{M-m} \frac{\eta^\ell}{\ell!} \sum_{n=1}^{N} \Phi_n^{(m)}(t) \frac{\partial^{\ell+1} \Psi_n(x, y, z)}{\partial z^{\ell+1}}\bigg|_{z=0} \right]^2. \tag{2.14}$$

Here, $\nabla_h = (\partial/\partial x, \partial/\partial y)$ is the horizontal gradient. For the deep-water waves considered in this study, $\Psi_n(x, y, z) = \exp(|\boldsymbol{k}(n)|z + \mathrm{i}\boldsymbol{k}(n) \cdot \boldsymbol{x})$, where $\boldsymbol{k}(n) = (k_x(n), k_y(n))$ is the wavenumber vector for the nth eigenfunction mode and $\mathrm{i} = \sqrt{-1}$. The relation between the scalar wavenumber k (see § 3) and the wavenumber vector is $k = |\boldsymbol{k}| = \sqrt{k_x^2 + k_y^2}$. A pseudo-spectral method with Fourier series is used for spatial discretization. A fourth-order Runge–Kutta scheme is used to advance (2.13) and (2.14) in time.

The HOSM is an accurate and efficient tool for the nonlinear wave simulation in a wave phase-resolved framework. It is capable of simulating a broadband wavefield with nonlinear wave–wave interactions being resolved to order M. It requires a computational cost proportional to $MN \log N$ only, and has an exponential convergence rate of the solution with respect to M and N. It has been applied to a wide range of wave problems. A complete review of the methodology, validation and application of the HOSM is provided by Mei *et al.* (2005, chap. 15).

Note that for the same horizontal resolution, the computational cost of HOSM simulation is much lower than that of the LES of wind turbulence. Therefore, without compromising the computational efficiency, HOSM simulations can be performed at the same horizontal resolution as the LES, such as in the LESns-R in this paper. Alternatively, HOSM simulations can be performed at higher horizontal resolution than

the LES, in order to obtain wave height distributions covering both the resolved (GS), and the dynamically important portion of SGS ranges of the wave spectrum, such as in the LESns-M applications to be undertaken.

At each time step of the wind and wave simulations, first the HOSM advances the wavefield in time; based on the result of HOSM, the surface geometry and velocity are provided to the wind LES, and the wind simulation advances in time. Specifically, in LESns-R, the wave surface elevation is used for grid mapping, and the surface velocity is used as a Dirichlet boundary condition for the velocity field. In LESns-M, in addition to grid mapping, the SGS part of the surface elevation from the HOSM is also used to calculate the sea-surface roughness. The surface-layer model gives the sea-surface stress as a Neumann condition for the wind velocity field based on the law of the wall. Details on how to calculate the SGS sea-surface roughness using the dynamic modelling approach and impose the sea-surface stress boundary condition are discussed in § 3. An example of the results of LESns-M and HOSM simulations is shown in figure 2.

Note that the above wind and wave simulation uses a one-way coupling scheme, in which the pressure and shear stress forcing from the wind to the wave is neglected. This is sufficient for the test of sea-surface roughness models in the present study. A more sophisticated two-way coupling approach is available in the current numerical framework, allowing the air pressure to force the evolution of the wavefield. However, for the simulation durations considered in the present study, the one-way and two-way couplings result in only small differences in the wavefield. The influence of such differences on the tests and validations of sea-surface roughness models is negligible. In future studies, when investigating the physics of wavefield evolution under wind forcing in more detail, two-way coupling between the wind and wave simulations will be used.

3. Dynamic SGS sea-surface roughness model for LES

3.1. *General idea and mathematical formulation*

Let $\widetilde{\eta}(x, y, t)$ be the sea-surface elevation filtered at the LES resolution Δ, and let $\widetilde{n}_i$ be the components of the unit vector normal to the filtered sea-surface elevation given by

$$\widetilde{n}_i(i = 1, 2, 3) = \frac{(-\widetilde{\eta}_x, -\widetilde{\eta}_y, 1)}{\sqrt{\widetilde{\eta}_x^2 + \widetilde{\eta}_y^2 + 1}}, \tag{3.1}$$

with the subscripts 'x' and 'y' denoting partial derivatives in the streamwise and spanwise directions, respectively. Then, the total drag acting on the wind at the sea surface is given as

$$F_i = -\iint_A \widetilde{p}^{\,s}\,\widetilde{n}_i \,\mathrm{d}x\,\mathrm{d}y + \rho_a \iint_A \tau_{ij,\Delta}^{SGS}\,\widetilde{n}_j \,\mathrm{d}x\,\mathrm{d}y, \quad i = 1, 2. \tag{3.2}$$

On the right-hand side of (3.2), the first and second terms represent the drag due to GS and SGS waves, respectively. It is assumed that the Reynolds number is large enough so that the viscous drag at scales Δ and larger is negligible. Here, A is the sea-surface area, $\widetilde{p}^{\,s}$ is the GS air pressure on the sea surface and ρ_a is the air density.

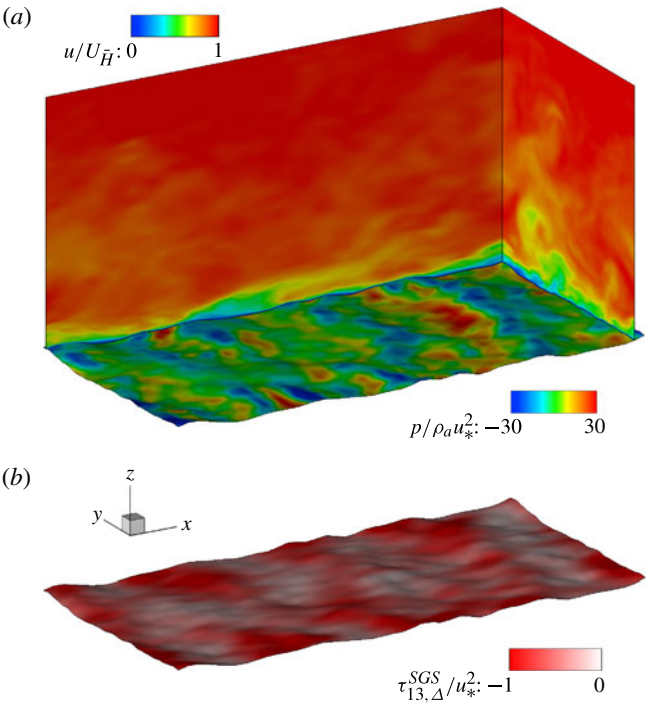

FIGURE 2. Illustration of LESns-M of wind turbulence together with HOSM simulations of wavefield for the CU6 case (the relevant parameters are given in table 1). In (*a*), contours of streamwise velocity (normalized by the mean velocity at the top of the simulation domain $U_{\widehat{H}}$) are plotted on two vertical planes, and contours of air pressure are plotted on the wave surface. In (*b*), contours of the instantaneous SGS surface shear stress $\tau^{SGS}_{13,\Delta}$ calculated by the wave-kinematics-dependent model are shown on the same wave surface as in (*a*).

The variable $\tau^{SGS}_{ij,\Delta}$ denotes the SGS kinematic surface stress. Its major components are modelled as (Moeng 1984; Albertson & Parlange 1999)

$$\tau^{SGS}_{i3,\Delta}(x,y,t) = -\left[\frac{\kappa \widehat{\widetilde{U}}_r(x,y,t)}{\log\left(d_2/z_{0,\Delta}\right)}\right]^2 \frac{\widehat{\widetilde{u}}_{r,i}(x,y,t)}{\widehat{\widetilde{U}}_r(x,y,t)}, \quad i=1,2. \tag{3.3}$$

Here, κ is the von Kármán constant, $\widehat{\widetilde{(\ldots)}}$ indicates filtering at test-filter scale $\widehat{\widetilde{\Delta}}$ ($\widehat{\widetilde{\Delta}} > \Delta$, e.g. $\widehat{\widetilde{\Delta}} = 2\Delta$), $z_{0,\Delta}$ is the roughness scale associated with SGS waves, $\widehat{\widetilde{u}}_{r,i}(x,y,t)$ is the air velocity relative to the water surface at the first off-surface grid point (i.e. in the LESns-M code to be used, at height d_2 above the sea surface), i.e.

$$\widehat{\widetilde{u}}_{r,i}(x,y,t) = \widehat{\widetilde{u}}_i(x,y,d_2,t) - \widehat{\widetilde{u}}_{s,i}(x,y,t), \tag{3.4}$$

with $\widehat{\widetilde{u}}_{s,i}(x,y,t)$ being the sea-surface velocity and

$$\widehat{\widetilde{U}}_r(x,y,t) = \sqrt{\left[\widehat{\widetilde{u}}_r(x,y,t)\right]^2 + \left[\widehat{\widetilde{v}}_r(x,y,t)\right]^2} \tag{3.5}$$

is the magnitude of $\widehat{\widetilde{u}}_{r,i}$.

We note that the logarithmic law in (3.3) was originally obtained in an averaged sense. To apply it locally, in (3.3) we use the test-filtered velocities at the scale $\widehat{\widetilde{\Delta}}$ instead of the grid-resolved velocities. As shown by Bou-Zeid, Meneveau & Parlange (2005), this filtering treatment reduces velocity fluctuations significantly and thus improves the applicability of (3.3). We also note that while there are fundamental limitations of the logarithmic law (e.g. the assumption of near-boundary equilibrium sometimes does not hold), we aim at mitigating these limitations by using dynamically determined parameters that can encode local dynamics that will be described on the resolved scales of the LES.

The SGS sea-surface roughness length $z_{0,\Delta}$ in (3.3) is modelled using a dynamic method following Anderson & Meneveau (2011),

$$z_{0,\Delta} = \sqrt{z_{0,s}^2 + (\alpha_w \sigma_\eta^\Delta)^2}. \tag{3.6}$$

Here, σ_η^Δ is the effective amplitude of the SGS waves, which is modelled on the basis of wave characteristics. (In Anderson & Meneveau (2011), σ_η^Δ is modelled as the r.m.s. value of SGS geometric height of land elevation.) The dimensionless coefficient α_w is, in principle, unknown but here it will be determined dynamically, allowing the surface roughness to vary with wind and wave conditions. For the wind and wave cases considered in the present study, $z_{0,s} \ll \alpha_w \sigma_\eta^\Delta$. As such, $z_{0,\Delta}$ is mainly determined by the dynamic roughness model part, $\alpha_w \sigma_\eta^\Delta$. The choice of the r.m.s. form in (3.6) over $\alpha_w \sigma_\eta^\Delta$ alone or the linear form in (1.1) is mainly for numerical convenience and also so that SGS height variances can be superposed linearly, rather than the r.m.s. values.

To determine the value of α_w, we consider two filter scales, Δ and $\widehat{\widetilde{\Delta}}$, and assume that the same α_w value holds at both scales (scale invariance of α_w). The constraint that the total drag force is independent of the resolution gives (Anderson & Meneveau 2011)

$$\begin{aligned}
&\iint_A \widetilde{p}^{\,s}\, \widetilde{n}_i \,\mathrm{d}x\,\mathrm{d}y + \rho_a \iint_A \left[\frac{\kappa \widehat{\widetilde{U}}_r}{\log\left(d_2/\sqrt{z_{0,s}^2 + (\alpha_w \sigma_\eta^\Delta)^2}\right)}\right]^2 \frac{\widehat{\widetilde{u}}_{r,i}}{\widehat{\widetilde{U}}_r}\,\mathrm{d}x\,\mathrm{d}y \\
&= \iint_A \widehat{\widetilde{p}}^{\,s}\, \widehat{\widetilde{n}}_i \,\mathrm{d}x\,\mathrm{d}y + \rho_a \iint_A \left[\frac{\kappa \overline{\widehat{\widetilde{U}}}_r}{\log\left(d_2/\sqrt{z_{0,s}^2 + (\alpha_w \sigma_\eta^{\widehat{\widetilde{\Delta}}})^2}\right)}\right]^2 \frac{\overline{\widehat{\widetilde{u}}}_{r,i}}{\overline{\widehat{\widetilde{U}}}_r}\,\mathrm{d}x\,\mathrm{d}y.
\end{aligned} \tag{3.7}$$

Here, $\overline{\widehat{\widetilde{(\ldots)}}}$ indicates filtering at a second test-filter scale $\overline{\widehat{\widetilde{\Delta}}}$ ($\overline{\widehat{\widetilde{\Delta}}} > \widehat{\widetilde{\Delta}} > \Delta$, e.g. $\overline{\widehat{\widetilde{\Delta}}} = 2\widehat{\widetilde{\Delta}} = 4\Delta$) and $\overline{\widehat{\widetilde{U}}}_r = \sqrt{(\overline{\widehat{\widetilde{u}}}_r)^2 + (\overline{\widehat{\widetilde{v}}}_r)^2}$. By solving (3.7), we obtain the value of α_w. In practice, there exist a variety of numerical algorithms for solving (3.7) (see, e.g., Kincaid & Cheney 2001). In the present study, equation (3.7) is solved by the bisection method, which was also used by Anderson & Meneveau (2011) with good performance.

In this study, we consider the case that the dominant waves propagate in the mean wind direction. Therefore, the condition (3.7) is enforced in the dominant flow direction (i.e. $i = 1$). As pointed out by Anderson & Meneveau (2011), if necessary, directional effects can be addressed by enforcing the vector equation using a

least-square error minimization over the two components. Furthermore, the integration area A can be either the entire computational surface if the globally averaged surface drag is the focus of the study, or local areas so that the sea-surface roughness can capture the spatial variations of the surface characteristics (Bou-Zeid, Parlange & Meneveau 2006). For an initial application of the dynamic roughness model to LES of wind–wave interactions, in this work we perform planar averaging over the entire computational surface.

3.2. *Models for the effective SGS surface wave amplitude* σ_η^Δ

A challenge in the present study is the modelling of the effective SGS wave amplitude of the sea surface, σ_η^Δ, which needs to be related to the characteristics of the waves. This subsection presents five possible choices, which cover different aspects of the wave properties.

In this study, we consider the height spectrum of the wind-generated sea-surface waves obtained during the Joint North Sea Wave Observation Project (JONSWAP) (Hasselmann *et al.* 1973), with its one-dimensional form in wavenumber space given by

$$F_J(k) = \frac{\alpha_J}{2k^3} \exp\left[-\frac{5}{4}\left(\frac{k_p}{k}\right)^2\right] \gamma^r. \tag{3.8}$$

Here, k is the wavenumber, k_p is the wavenumber of the spectrum peak and α_J, γ and r are parameters. Details of the JONSWAP spectrum, including the values of the parameters, are given in Appendix.

The directional spectrum $S(k,\theta)$ to be used in characterizing the wavefield is based on the one-dimensional spectrum (3.8) and a spreading function $D(k,\theta)$, according to

$$S(k,\theta) = D(k,\theta)\ F_J(k), \tag{3.9}$$

where the directional spreading function is given by (Cartwright 1963; Hasselmann, Dunckel & Ewing 1980)

$$D(k,\theta) = \begin{cases} N(s)\cos^{2s}\left(\dfrac{\pi}{\Theta}\theta\right), & |\theta| \leqslant \dfrac{\Theta}{2}, \\ 0, & |\theta| > \dfrac{\Theta}{2}. \end{cases} \tag{3.10}$$

Here, Θ is the range of the spreading angle, s is the spreading parameter and $N(s)$ is the normalization constant, with which $D(k,\theta)$ satisfies the constraint

$$\int_{-\pi}^{\pi} D(k,\theta)\,\mathrm{d}\theta = 1. \tag{3.11}$$

In the present study, we use $\Theta = \pi$ and $s = 1$, which gives $N(s) = 2/\pi$ based on (3.11).

3.2.1. *RMS model*

The first model, the RMS model, was proposed by Anderson & Meneveau (2011) for fractal-like (static) land surfaces. In this model, the r.m.s. value of SGS height fluctuations is used to model the surface roughness, i.e.

$$\sigma_\eta^\Delta = (\widetilde{\eta^2} - \tilde{\eta}^2)^{1/2}. \tag{3.12}$$

For a given spectrum $S(k, \theta)$, this becomes

$$\sigma_\eta^\Delta = \left[\int_{-\pi/2}^{\pi/2} \int_{\pi/\Delta}^{2\pi/\lambda_c} S(k, \theta)\, \mathrm{d}k\, \mathrm{d}\theta \right]^{1/2}, \tag{3.13}$$

where λ_c is the critical wavelength that separates gravity and capillary waves (Lamb 1932). Previous studies (e.g. Caudal 1993; Makin *et al.* 1995) have shown that the waves shorter than λ_c have a relatively small contribution to the total sea-surface stress and are thus neglected here.

This RMS model has been shown to produce satisfactory results for LES of wind over land surfaces (Anderson & Meneveau 2011). For wind over water waves, the surface roughness elements (i.e. waves) of different length scales have different propagation speeds. That is, relatively short waves propagate relatively slowly according to the deep-water dispersion relation

$$c(k) = \sqrt{g\lambda(k)/2\pi} = \sqrt{g/k}, \tag{3.14}$$

where $c(k)$ and $\lambda(k)$ are the phase speed and wavelength of the wave with wavenumber k, respectively. Previous studies have shown that the wave-induced form drag varies with the ratio of wave phase speed to wind velocity, called the wave age (see the reviews by Belcher & Hunt (1998), Cavaleri *et al.* (2007) and Sullivan & McWilliams (2010)). Therefore, the effect of wave propagation on surface roughness needs to be considered, which is lacking in the RMS model. As a consequence, the RMS model is expected to perform reasonably well only if the grid resolution is fine (i.e. Δ is small), so that the SGS waves propagate relatively slowly and can be approximated as static roughness elements.

To improve the model performance, revisions of (3.13) using weighted integration are considered in the next four models. Because long waves propagate faster than short waves and thus have less relative velocity with respect to the wind, less weight put on low k is needed in the integration.

3.2.2. *Geometry model*

The second model, geometry model, parameterizes the sea-surface roughness based on the geometry of the waves. This model follows Lettau's (1969) idea about the land surface roughness induced by rocks and sands, and was applied to ocean wavefield by Byrne (1982). It assumes that for a wave component with wavenumber k, the corresponding roughness is

$$z_0(k) = \alpha'_{w,B} H(k) \frac{A_{si}(k)}{A_{sp}(k)}. \tag{3.15}$$

Here, $\alpha'_{w,B}$ is a coefficient, $H(k)$ is the wave height, which is equal to twice the wave amplitude $a(k)$, and $A_{si}(k)$ and $A_{sp}(k)$ are the silhouette area and specific area (Lettau 1969) of the wave component, respectively. The ratio $A_{si}(k)/A_{sp}(k)$ can be expressed as (Byrne 1982)

$$\frac{A_{si}(k)}{A_{sp}(k)} = \frac{H(k)}{\lambda(k)} = \frac{kH(k)}{2\pi}. \tag{3.16}$$

Substituting (3.16) into (3.15) gives

$$z_0(k) = \frac{\alpha'_{w,B} kH(k)^2}{2\pi} = \alpha_{w,B} kH(k)^2. \tag{3.17}$$

Therefore, for a wave spectrum $S(k,\theta)$, the effective amplitude of the SGS waves is

$$\sigma_\eta^\Delta = \int_{-\pi/2}^{\pi/2}\int_{\pi/\Delta}^{2\pi/\lambda_c} kS(k,\theta)\,\mathrm{d}k\,\mathrm{d}\theta, \tag{3.18}$$

where any scalar prefactor is omitted since it is considered to be absorbed into the coefficient α_w to be determined dynamically. Similar to the RMS model, the geometry model treats the waves as static roughness element and lacks wave kinematics. Nevertheless, the integrand is weighted by k.

3.2.3. *Steepness-dependent Charnock model*

The third model, the steepness-dependent Charnock model, originated from Hsu (1974). For a wave component with wavenumber k, it is assumed that the Charnock coefficient α_{ch} in (1.2) is dependent on wave steepness:

$$\alpha_{ch} = \alpha_{w,H}\frac{H(k)}{\lambda(k)} = \alpha_{w,H}\frac{kH(k)}{2\pi}, \tag{3.19}$$

where $\alpha_{w,H}$ is a coefficient. Substituting (3.19) into (1.2) gives

$$z_0 = \alpha_{w,H}kH(k)\frac{u_*^2}{2\pi g}. \tag{3.20}$$

For a wave spectrum $S(k,\theta)$, this yields a model for the effective amplitude of the SGS waves

$$\sigma_\eta^\Delta = \left[2\int_{-\pi/2}^{\pi/2}\int_{\pi/\Delta}^{2\pi/\lambda_c} k^2S(k,\theta)\,\mathrm{d}k\,\mathrm{d}\theta\right]^{1/2}\frac{u_*^2}{2\pi g}. \tag{3.21}$$

Note that the integrand $k^2S(k,\theta)$ is the slope spectrum of the wavefield (Janssen 2004). Compared with the RMS model in (3.13) and the geometry model in (3.18), the steepness-dependent Charnock model puts more weight on the high wavenumber modes, and thus highlights the effect of short waves on the sea-surface roughness.

3.2.4. *Wave-kinematics-dependent model*

The fourth model, the wave-kinematics-dependent model, originated from Kitaigorodskii & Volkov (1965) and was later generalized to a continuous wave spectrum by Kitaigorodskii (1968) (for a review, see Donelan 1990). For a wave mode with wavenumber k, the logarithmic law of the velocity profile in the frame of reference moving with the wave is assumed to be

$$\frac{U(z)-c(k)}{u_*} = \frac{1}{\kappa}\log\frac{z}{\alpha a(k)}. \tag{3.22}$$

Here, α is a model parameter. Using the dispersion relation for deep water waves, $c(k)=\sqrt{g/k}$, (3.22) is rewritten as

$$\frac{U(z)}{u_*} = \frac{1}{\kappa}\log\frac{z}{\alpha a(k)\exp\left(-(\kappa/u_*)\sqrt{g/k}\right)}. \tag{3.23}$$

Therefore,

$$z_0(k) = \alpha a(k)\exp[-(\kappa/u_*)\sqrt{g/k}], \tag{3.24}$$

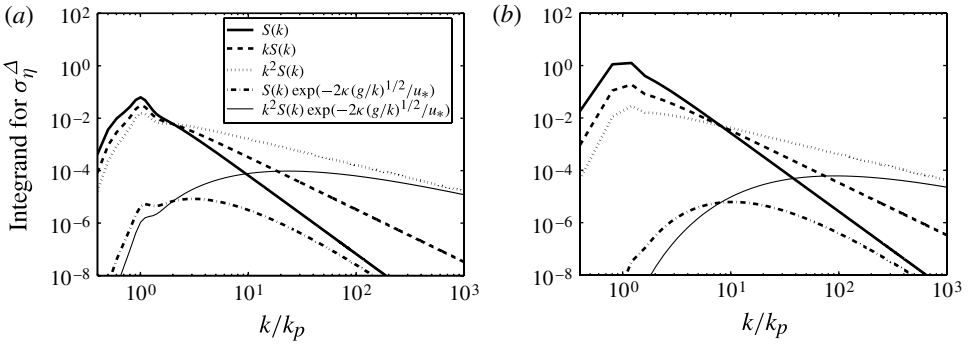

FIGURE 3. The integrands in the modelling of σ_η^Δ as functions of k/k_p: thick solid line, RMS model (equation (3.13)); dashed line, geometry model (equation (3.18)); dotted, steepness-dependent Charnock model (equation (3.21)); dash–dotted line, wave-kinematics-dependent model (equation (3.25)); and thin solid line, combined-kinematics-steepness model (equation (3.26)). The wave spectra $S(k,\theta)$ are based on the JONSWAP wave spectrum with a wind speed of $U_{10} = 10.0\ \mathrm{m\ s^{-1}}$ and fetch values of (*a*) $F = 10$ km and (*b*) $F = 80$ km. The values of k_p are 0.48 and 0.12 $\mathrm{m^{-1}}$ in (*a*,*b*), respectively. Note that the integrands have different dimensions and it is thus inappropriate to compare them directly. The purpose of the plot is to show their variations with k with different weights.

and the corresponding superposition of wave amplitudes based on a wave spectrum $S(k,\theta)$ (Kitaigorodskii 1968) can be written as

$$\sigma_\eta^\Delta = \left[\int_{-\pi/2}^{\pi/2}\int_{\pi/\Delta}^{2\pi/\lambda_c} S(k,\theta)\exp\left(-\frac{2\kappa}{u_*}\sqrt{\frac{g}{k}}\right)\mathrm{d}k\,\mathrm{d}\theta\right]^{1/2}. \tag{3.25}$$

Note that the function $\exp[-2(\kappa/u_*)\sqrt{g/k}\,]$ approaches 0 as $k \to 0$ and approaches 1 as $k \to \infty$. Therefore, the wave-kinematics-dependent model emphasizes the contribution of short waves to sea-surface roughness by reducing the weights of long waves.

3.2.5. *Combined-kinematics-steepness model*

The fifth model, the combined-kinematics-steepness model, combines the ideas of the wave-kinematics-dependent model and the steepness-dependent Charnock model. Geernaert (1983) suggested the replacement of the vertical length scale $H(k)$ in (3.20) with the length scale given by (3.24). For a wave spectrum $S(k,\theta)$, we have

$$\sigma_\eta^\Delta = \left[\int_{-\pi/2}^{\pi/2}\int_{\pi/\Delta}^{2\pi/\lambda_c} k^2S(k,\theta)\exp\left(-\frac{2\kappa}{u_*}\sqrt{\frac{g}{k}}\right)\mathrm{d}k\,\mathrm{d}\theta\right]^{1/2}\frac{u_*^2}{2\pi g}. \tag{3.26}$$

Figure 3 illustrates the shape of the integrands of each σ_η^Δ model, namely S in the RMS model (equation (3.13)), kS in the geometry model (equation (3.18)), k^2S in the steepness-dependent Charnock model (equation (3.21)), $S\exp(-2\kappa/u_*\sqrt{g/k})$ in the wave-kinematics-dependent model (equation (3.25)) and $k^2S\exp(-2\kappa/u_*\sqrt{g/k})$ in the combined-kinematics-steepness model (equation (3.26)). As shown, in different models, different weights are put on the integration of the wave spectrum. As pointed out earlier, short waves propagate relatively slowly and thus are more effective in exerting drag on the wind. In the subsequent sections, we assess which model performs best.

It should be clarified that in the models discussed here, the addition associated with the integrals in the modelling of σ_η^Δ is not meant to represent additive contributions to the stress by simple superposition of the square of the length scales. Instead, the additivity refers to an attempt to describe the geometry of the surface using a single length scale in a way that becomes additive when more scales are added. To relate to hydrodynamic forces, we then assume that the proposed dynamic determination of the parameter α_w effectively accounts for the combined effects of the discarded small scales. Such a dynamic modelling approach, as shown in the next section, is found to be capable of capturing the essential characteristics of the SGS sea-surface roughness and impose proper SGS surface stress on the LES.

4. Results

4.1. *LESns-R results*

We perform LESns-R on a fine grid to obtain high-resolution benchmark data for the *a priori* tests as well as for subsequent *a posteriori* tests on coarser grids. For LESns-R of wind turbulence, we consider a simulation domain with a size of $(L_x, L_y, \overline{H}) = (2\lambda_p, \lambda_p, \lambda_p)$. For the simulation of turbulence over waves, such a domain size has been found to be sufficient for applying the periodic boundary condition in the horizontal directions and free-slip condition at the top of the domain (e.g. Henn & Sykes 1999; Calhoun, Street & Koseff 2001; Yang & Shen 2009). We use a grid resolution of $(N_x, N_y, N_z) = (128, 256, 64)$ with evenly distributed grid points in the horizontal directions and clustered grid towards the wave surface in the vertical direction. With the 2/3 rule for dealiasing in the horizontal directions, the current resolution provides 85 and 170 aliasing-free effective grid points in x and y directions, respectively. Note that for LESns-R, the grid resolution should satisfy $\Delta x^+ \lesssim 100$, $\Delta y^+ \lesssim 20$ and $\Delta z^+ \lesssim 2$ near the boundary in order to resolve the streaky structures and viscous sublayer (Piomelli & Balaras 2002). Here, the superscript '+' denotes the length normalized by the wall unit length ν_a/u_*. We use a moderately low Reynolds number, $Re_* = u_*\lambda_p/\nu_a = 4096$, since, as is well known, resolving the surface layer precludes simulating realistically high Reynolds numbers. Based on $Re_* = 4096$ we have $\Delta x^+ = 64.0$ and $\Delta y^+ = 16.0$. The vertical grid size is $\Delta z^+ = 2.0$ near the wave surface and gradually increases to $\Delta z^+ = 118.6$ towards the top of the simulation domain. The simulation time step is $\Delta t^+ = 0.04$, which is sufficiently small to capture the evolution of resolved eddies and to meet the requirement of the numerical stability of the time integration scheme.

For the wavefield, we consider JONSWAP wave spectra. By varying the value of fetch F, three JONSWAP wave spectra with various peak phase speeds are obtained. The key parameters of the wave spectra are given in table 1. Based on these parameters and (3.8) and (3.10), the ocean broadband wavefield for the HOSM simulation is generated using a random phase method (Wu 2004). A horizontal resolution of $(N_x, N_y) = (128, 256)$ is used for the HOSM. The one-dimensional wave surface elevation spectra $F_J(k)$ obtained from the simulations are plotted in figure 4. Plotted are the mean wave elevation spectra averaged over 50 peak wave periods. When normalized by g/u_*^2 (figure 4*a*), the spectra for all of the three cases collapse well in the high wavenumber range, and show a -3 slope when plotted in logarithmic scales. The vertical shift of the spectra when normalized by k_p (figure 4*b*) is expected, and is caused by the change of fetch (see (A 1) and (A 3) in the Appendix).

To understand the sea-surface drag on wind and the momentum transfer between wind and waves, it is essential to quantify the air pressure applied at the wave

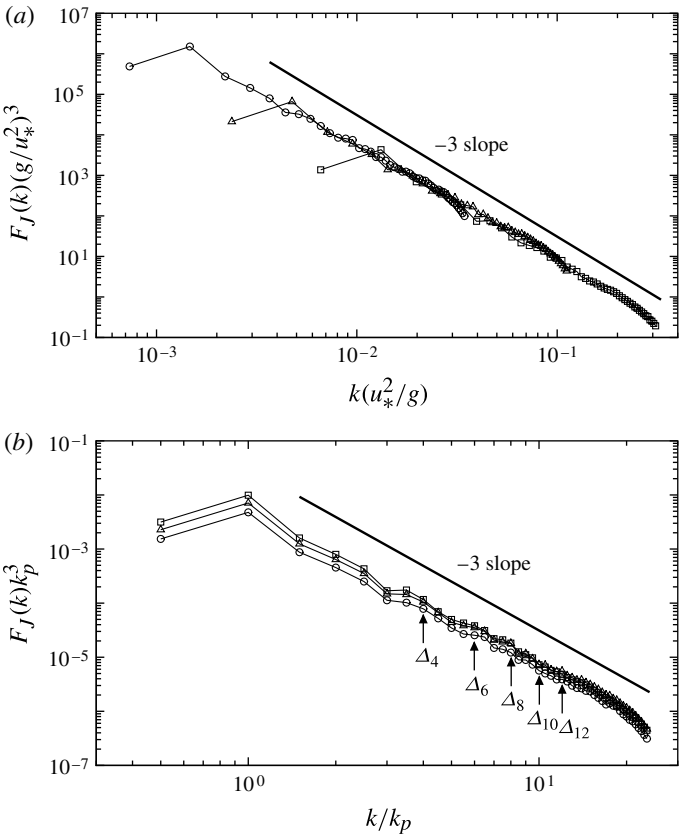

FIGURE 4. One-dimensional wavenumber spectra of surface elevation for the JONSWAP wavefields simulated by HOSM: □, case CU6; △, case CU10; and ◯, case CU18. Variables in (*a*) are normalized by the wind friction velocity u_* and gravitational acceleration g; variables in (*b*) are normalized by the peak wavenumber k_p. The corresponding locations of filters Δ_4, Δ_6, Δ_8, Δ_{10} and Δ_{12} used for *a priori* tests are also indicated in (*b*).

Case	U_{10} (m s^{-1})	F (m)	c_p (m s^{-1})	c_p/u_*	λ_p (m)	k_p (m^{-1})
CU6	12	1707.6	2.66	6	4.54	1.38
CU10	12	7905.5	4.43	10	12.62	0.50
CU18	12	46104.9	7.99	18	40.88	0.15

TABLE 1. Parameters of JONSWAP spectra for the HOSM simulations.

surface for different wave components. A desired approach is to perform two-dimensional Fourier transform for the surface wave elevation and air pressure distribution, and then calculate the directional wave growth rate. However, because the air pressure has large fluctuations associated with wave-induced variations and turbulence fluctuations, a large number of data samples are required for statistically converged result of the directional wave growth rate. This is unaffordable with the computer resources available to us at present due to the high computational cost of

LESns-R. Alternatively, we focus on one-dimensional result by first performing Fourier transform in the streamwise direction and then performing ensemble averaging in the spanwise direction. The availability of 256 grid lines at different spanwise locations substantially improves the quality of statistical results. Note that the focus on the streamwise direction can be justified by the fact that the waves primarily propagate in that direction and the wave growth rate does not have large variations within moderate spreading angles where the majority of wave energy exists. Moreover, this approach is consistent with the one-dimensional form of existing experimental and theoretical results used for comparison and validation in the study.

We decompose the air pressure into different wave modes corresponding to different wavenumbers k. The temporal rate of energy transfer from the wind to the wave at wavenumber k is quantified as (Donelan *et al.* 2006)

$$\gamma(k) = \frac{\rho_w}{\rho_a}\frac{1}{\omega(k)e(k)}\frac{\mathrm{d}e(k)}{\mathrm{d}t} = \left(\frac{u_*}{c(k)}\right)^2 \beta(k). \tag{4.1}$$

Here, for the kth mode, $e(k) = \rho_w g[a(k)]^2/2$ is the wave energy density, $\omega(k) = \sqrt{gk}$ is the corresponding angular frequency for deep water waves and $\beta(k)$ is the wave growth rate parameter (Miles 1957, 1993). Under wind forcing, wind and wave exchange momentum and energy mainly through form drag (see, e.g., the reviews by Belcher & Hunt (1998) and Sullivan & McWilliams (2010)). The growth rate parameter $\beta(k)$ is related to the wind forcing through (see, e.g., Donelan *et al.* 2006)

$$\beta(k) = \frac{2D_p(k)}{[a(k)k]^2}, \tag{4.2}$$

where

$$D_p(k) = \frac{1}{A}\iint_A \frac{p_k}{\rho_a u_*^2}\frac{\partial \eta_k}{\partial x}\,\mathrm{d}x\,\mathrm{d}y \tag{4.3}$$

is the normalized streamwise form drag per unit area for wave mode k, with p_k and η_k being the corresponding air pressure at the wave surface and surface displacement, respectively.

Figure 5 shows the values of β for different wave modes. As shown in figure 5(a), for cases CU6 and CU10, β has a nearly constant value of 25 over the resolved scale in LESns-R. For case CU18 where the waves are relatively mature, the value of β increases from -3 near the spectrum's peak to 21 at high wavenumbers. For cases CU6 and CU10 where the waves are younger than those in CU18, β is positive and large. When plotted as a function of the dimensional wavenumber k (figure 5b), the values of β from these three cases converge better and indicate a slightly negative value for long waves (small k) and a nearly constant positive value for short waves (large k), consistent with previous studies (see, e.g., the reviews of Belcher & Hunt (1998) and Cavaleri *et al.* (2007)). We note that among the different cases, the values of β differ at small k and collapses at large k. This phenomenon is consistent with the common behaviour of turbulence: large-scale motions differ among different flows, while small-scale motions are more universal. In the current problem of wind over waves, the turbulence wind field is affected by the broadband waves in a complex way. Using LES to explicitly resolve the GS eddies and wave components seems a good approach. For the modelling of SGS effects, such as the SGS surface roughness studied in the present paper, it is the stress at the scales near the grid size Δ and the

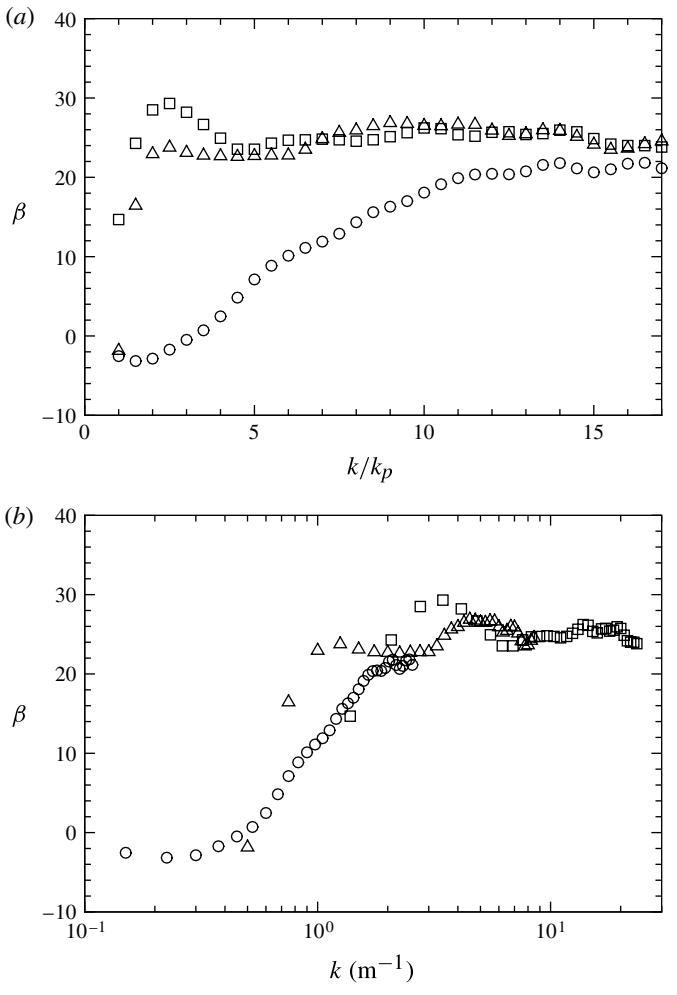

FIGURE 5. Values of the wave growth rate parameter β for different wave modes. In (*a*), β is plotted as a function of dimensionless wavenumber k/k_p, where k_p is the wavenumber of the spectrum peak. In (*b*), β is plotted as a function of dimensional wavenumber k (m^{-1}) on a semi-logarithmic scale. LESns-R results for various wind–wave cases are plotted: □, case CU6; △, case CU10; and ◯, case CU18.

test-filter size $\widehat{\widehat{\Delta}}$ that matter most for the dynamic modelling. As shown in figure 5(*b*), the three cases have consistent results at large k corresponding to Δ and $\widehat{\widehat{\Delta}}$, suggesting the suitability of the data to be used for the test of SGS surface roughness models.

In the literature, β is often parameterized as a function of wave age c/u_*. Figure 6 shows the dependence of β on c/u_*, and compares the current LESns-R results with previous numerical and theoretical results. As c/u_* increases from 0, β increases first, reaches its maximal value around $c/u_* = 5$ and then decreases as c/u_* increases further. The results obtained by the current LESns-R agree with previous numerical results. At small c/u_*, our LESns-R result falls in the middle of various theoretical predictions. At large c/u_*, the numerical result agrees with the rapid-distortion theory by Cohen & Belcher (1999) better than with the other three predictions based on

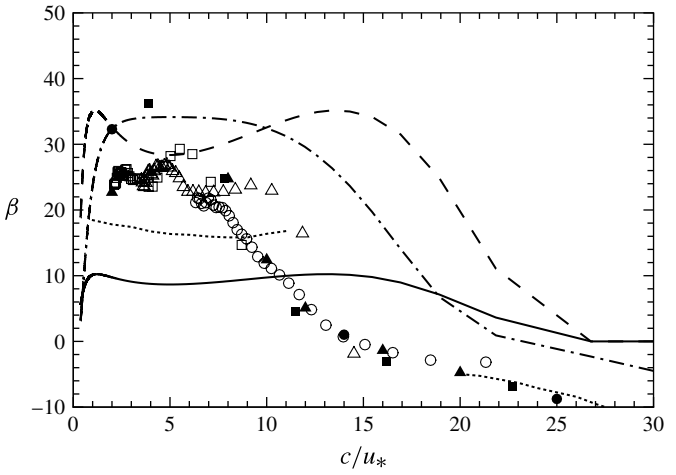

FIGURE 6. Dependence of wave growth rate parameter β on wave age c/u_*. Values predicted by various theories are indicated by lines: ——, Miles (1957); − −, Janssen (1991); − · −, Miles (1993); and · · ·, Cohen & Belcher (1999). Results from previous numerical studies are indicated by solid symbols: ■, Sullivan *et al.* (2000); ▲, Kihara *et al.* (2007); and ●, Yang & Shen (2010). Values obtained by the current LESns-R are indicated by open symbols: □, case CU6; △, case CU10; and ◯, case CU18.

the critical-layer theory (Miles 1957, 1993; Janssen 1991), because Cohen & Belcher (1999) considered relatively more details of the wind turbulence structure. Cohen & Belcher (1999) also predicted negative values of β for $c/u_* > 20$. Note that in figure 6, the line for Cohen & Belcher (1999) consists of two parts, one for $c/u_* < 11$ and the other for $c/u_* > 20$, corresponding to slow and fast waves, respectively. Moreover, in figure 6, the numerical studies of Sullivan *et al.* (2000), Kihara *et al.* (2007) and Yang & Shen (2010) are for monochromatic waves, while the current LESns-R is for broadband waves.

Figure 7 shows the dependence of the temporal growth rate γ on the reversed wave age u_*/c in a logarithmic scale. Note that the dispersion relation gives $u_*/c = \omega u_*/g$. As a result, the reversed wave age is also a dimensionless angular frequency of the wave, $\omega_* = \omega u_*/g$. Figure 7 shows that short waves (which have large frequencies) grow faster than long waves (Plant 1982). The results from the three cases of the current LESns-R collapse, and agree quite well with previous experimental, theoretical and numerical data in the literature.

Note that the current LESns-R uses, by necessity, a fairly low value of the Reynolds number, namely $Re_* = u_*\lambda_p/\nu = 4096$. It is set to be lower than geophysically relevant values for the purpose of resolving the near-surface region. To investigate the Reynolds number effect and to assure that the value used in our study is not too low to subtract validity to our test result, we have performed an additional simulation for case CU10 but with a reduced Reynolds number of $Re_* = 1264$. We denote this case as CU10-LR. Figure 8 compares γ between cases CU10 and CU10-LR. As shown, the values of γ obtained from case CU10-LR agree well with those from case CU10 up to $k/k_p = 9$. At higher k, the results become different, with the γ from case CU10-LR exhibiting a reduction, indicating viscous effect at $k/k_p > 9$. Unlike case CU10-LR, the other three cases, CU6, CU10 and CU18, do not show the Reynolds number effect of

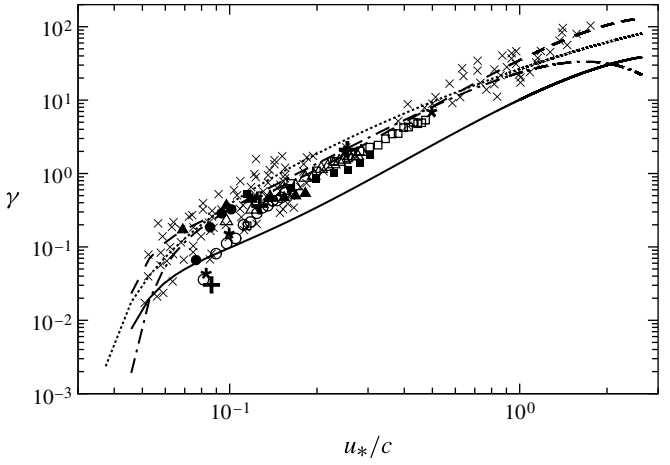

FIGURE 7. Dependence of wave temporal growth rate γ on reversed wave age u_*/c and comparison of the current LESns-R with previous experiments and simulations. Experimental data compiled by Plant (1982) are indicated by $\times$. Predictions by various wind–wave theories are indicated by lines: ——, Miles (1957); − −, Janssen (1991); and − · −, Miles (1993). Parameterization by Donelan *et al.* (2006) is indicated by · · · . DNS results from Sullivan *et al.* (2000) are marked by $+$. DNS results from Kihara *et al.* (2007) are marked by $\star$. Values obtained by the current LESns-R are indicated by open symbols: □, case CU6; △, case CU10; and ◯, case CU18. Values obtained by the current dynamic surface-modelled approach (LESns-M) with the wave-kinematics-dependent model for σ_η^Δ are indicated by solid symbols: ■, case CU6; ▲, case CU10; and ●, case CU18.

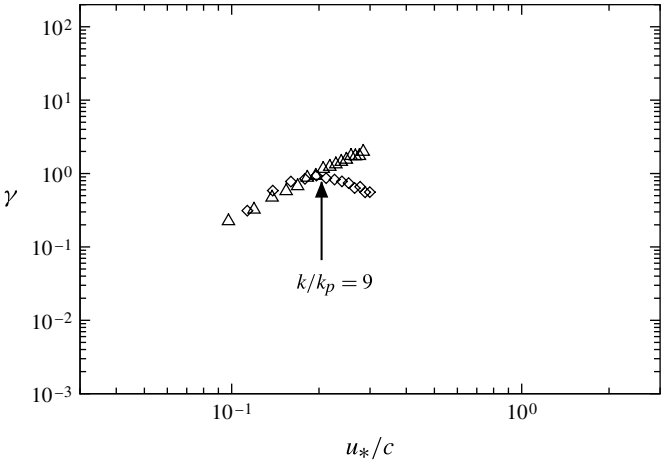

FIGURE 8. Similar to figure 7 but for the illustration of Reynolds number effect: △, case CU10 with $Re_* = 4096$; and ◇, case CU10-LR with $Re_* = 1264$. The corresponding location of Δ_9 ($k/k_p = 9$) is indicated in the figure.

decreasing γ in figure 7. Therefore, while caution should be taken in using LESns-R for the SGS model test if the Reynolds number is too low, such as in case CU10-LR, the three cases used in this study are still valid.

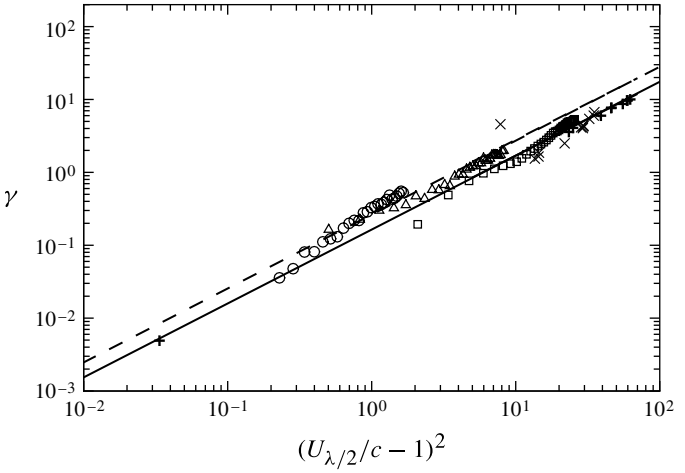

FIGURE 9. Scaling of the temporal wave growth rate γ with the mean wind velocity at the height of half wavelength. Experimental data by Donelan (1999) are indicated by $\times$. Parameterizations based on experimental data are shown by lines: $- - -$, $\gamma = 0.28(U_{\lambda/2}/c-1)^2$ by Donelan (1999) based on laboratory data; and ——, $\gamma = 0.17(U_{\lambda/2}/c-1)^2$ by Donelan *et al.* (2006) based on field data. DNS results of Yang & Shen (2010) are indicated by $+$. Values obtained by the current LESns-R are indicated by open symbols: $\square$, case CU6; $\triangle$, case CU10; and $\bigcirc$, case CU18.

Donelan *et al.* (2006) analysed the field measurement data obtained from wave-following probes, and suggested that the wave growth rate may scale better with $U_{\lambda/2}$ than with u_*, where $U_{\lambda/2}$ is the mean wind velocity at the height of $\lambda/2$ above the wave surface for a given wave mode. This scaling was supported by the recent numerical study of turbulence over monochromatic waves by Yang & Shen (2010). In figure 9, the values of $\gamma(k)$ obtained by the current LESns-R simulation with broadband waves are plotted as a function of $(U_{\lambda/2}/c-1)^2$, with $U_{\lambda/2}$ now being the mean wind velocity at the height of $\lambda(k)/2$ for the corresponding wave mode with wavenumber k. The current results show good scaling of γ with $U_{\lambda/2}$, and agree with the parameterizations of Donelan (1999) and Donelan *et al.* (2006) and the simulation results of Yang & Shen (2010). A comparison between figures 7 and 9 indicates that the variance of γ when scaled with $U_{\lambda/2}$ is indeed smaller than that when scaled with u_*.

The analyses and comparisons in this section indicate that the current LESns-R captures the essential physics of the interactions of wind turbulence with broadband sea-surface waves. Therefore, in the subsequent sections, the results of these LESns-R are used as database for the *a priori* and *a posteriori* tests of the dynamic sea-surface roughness models developed in § 3.

4.2. *A priori tests of dynamic sea-surface roughness models*

In *a priori* tests, the data of LESns-R at fine grid resolution is filtered to coarse grids to evaluate the roughness models discussed in § 3. A variety of filter sizes are considered, which are listed in table 2. The spectral positions for some of the filters are indicated in figure 4.

The dynamic method discussed in § 3.1 involves finding the roughness index α_w that solves (3.7) (the equation expresses the first-principles constraint of resolution-

		Filter size Δ (m)		
Filter	k_Δ/k_p	CU6	CU10	CU18
Δ_4	4	1.14	3.16	10.22
Δ_5	5	0.91	2.52	8.18
Δ_6	6	0.76	2.10	6.81
Δ_7	7	0.65	1.80	5.84
Δ_8	8	0.57	1.58	5.11
Δ_9	9	0.50	1.58	4.54
Δ_{10}	10	0.45	1.40	4.09
Δ_{11}	11	0.41	1.26	3.72
Δ_{12}	12	0.38	1.05	3.41

TABLE 2. Filter sizes for *a priori* tests.

independent total drag force). Note that the SGS surface stress depends on the value of α_w, so does the total surface stress. For the grid filter of size Δ, the plane-averaged total surface stress, which is the sum of GS and SGS surface stresses, is

$$\langle \tau_{13}^{T,\Delta} \rangle(\alpha_w) = -\frac{1}{\rho_a}\langle \widetilde{p}^s \widetilde{n}_1 \rangle - \left\langle \left[\frac{\kappa \widehat{\widetilde{U}}_r}{\log\left(d_2 / \sqrt{z_{0,s}^2 + (\alpha_w \sigma_\eta^\Delta)^2} \right)} \right]^2 \frac{\widehat{\widetilde{u}}_{r,1}}{\widehat{\widetilde{U}}_r} \right\rangle, \tag{4.4}$$

where $\langle \cdots \rangle$ indicates two-dimensional plane-averaging, and the superscript 'T' denotes total. When $\alpha_w = 0$, (4.4) gives the total surface stress on a smooth, wavy surface with all of the form drag captured by the GS surface pressure variation. As shown in figure 10, when α_w increases, the total surface stress increases with the additional contribution of form drag due to SGS surface waves. As introduced in § 3.1, with an additional test filter with size $\widehat{\widetilde{\Delta}}$, the intersect of the $\langle \tau_{13}^{T,\Delta} \rangle(\alpha_w)$ curve and the $\langle \tau_{13}^{T,\widehat{\widetilde{\Delta}}} \rangle(\alpha_w)$ curve gives the value of α_w as the solution of (3.7).

In figure 10, examples of $\langle \tau_{13}^{T,\Delta} \rangle(\alpha_w)$ and $\langle \tau_{13}^{T,\widehat{\widetilde{\Delta}}} \rangle(\alpha_w)$ are shown for all of the five σ_η^Δ models proposed in § 3.2. Also plotted is the benchmark line of $-\langle \tau_{13}^T \rangle = u_*^2$, which follows from overall momentum balance in statistically stationary equilibrium, when the pressure force applied to the wind must be on average balanced by the surface drag on the bottom surface. Figure 10 indicates that the dynamic procedure described by (3.7) generates a single and stable solution for the model coefficient α_w, in the context of all of the five models of σ_η^Δ considered. Meanwhile, there exist different levels of agreement with the additional overall momentum constraint $-\langle \tau_{13}^T \rangle = u_*^2$ among these models. Evidently the wave-kinematics-dependent model yields the best result. The RMS model and the geometry model underestimate the values of α_w and SGS surface stress. The steepness-dependent Charnock model provides the second best result, with the prediction of the total surface stress slightly higher than the benchmark value. The combined-kinematics-steepness model overestimates the surface stress.

It is important to point out that the results from these *a priori* tests do not mean that in actual LES using the four less satisfactory σ_η^Δ models, there will be a mismatch between applied pressure and surface drag. In actual LES, a new equilibrium develops

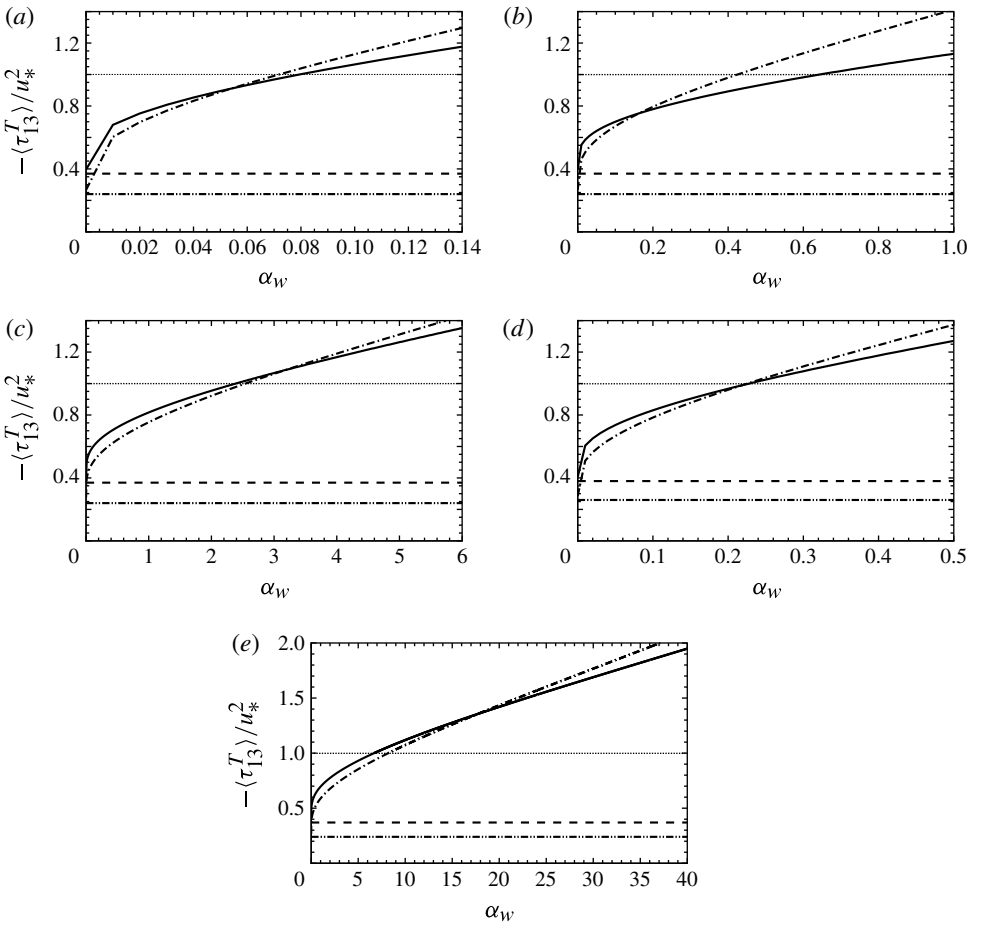

FIGURE 10. Total and resolved surface stresses as functions of roughness index α_w. The surface stresses are normalized by u_*^2. In the *a priori* test, the grid-filter size is set to be $\Delta = \Delta_{12}$ and the test-filter size is set to be $\widehat{\widetilde{\Delta}} = \Delta_8$. Values corresponding to Δ are indicated by: —, total stress; and − − −, resolved stress. Values corresponding to $\widehat{\widetilde{\Delta}}$ are indicated by: − · −, total stress; and − · ·−, resolved stress. The results of various models for case CU6 are plotted: (*a*) RMS model; (*b*) geometry model; (*c*) steepness-dependent Charnock model; (*d*) wave-kinematics-dependent model; and (*e*) combined-kinematics-steepness model. The horizontal line of $-\langle\tau_{13}^T\rangle/u_*^2 = 1$ indicates the benchmark value of the total surface stress.

in which $-\langle\tau_{13}^T\rangle = u_*^2$, but the resolved fields can be expected to present less realistic statistics compared to those of the filtered LESns-R results.

To evaluate and understand the performance of each σ_η^Δ model, we use the data from the LESns-R to obtain benchmark values of σ_η^Δ at various filter sizes with the following procedure. If the turbulence and wave motions at all of the scales of interest are known, the total surface stress in the streamwise direction can be written as

$$\langle\tau_{13}^T\rangle = -u_*^2 \int_{-\pi/2}^{\pi/2} \int_0^{k_c} k^2 \beta(k) S(k,\theta) \cos^2\theta \, \mathrm{d}k \, \mathrm{d}\theta - \left[\frac{\kappa U_h}{\log(h/z_{0,s})}\right]^2, \tag{4.5}$$

where U_h is the mean wind velocity at $z = h$.

In LES, only the flow motions at scales larger than the grid-filter size Δ are resolved, and the total surface stress is written as

$$\langle \tau^{T}_{13,\Delta} \rangle = \langle \tau^{GS}_{13,\Delta} \rangle - \left[\frac{\kappa U_h}{\log(h/z_{0,\Delta})} \right]^2, \tag{4.6}$$

where

$$\langle \tau^{GS}_{13,\Delta} \rangle = -u_*^2 \int_{-\pi/2}^{\pi/2} \int_{0}^{\pi/\Delta} k^2 \beta(k) S(k,\theta) \cos^2\theta \, \mathrm{d}k \, \mathrm{d}\theta \tag{4.7}$$

is the contribution from the GS gravity waves. Because the total surface stress is independent of resolution, equalizing (4.5) and (4.6) gives

$$\langle \tau^{SGS}_{13,\Delta} \rangle = -u_*^2 \int_{-\pi/2}^{\pi/2} \int_{\pi/\Delta}^{k_c} k^2 \beta(k) S(k,\theta) \cos^2\theta \, \mathrm{d}k \, \mathrm{d}\theta \tag{4.8}$$

$$= \left[\frac{\kappa U_h}{\log(h/z_{0,s})} \right]^2 - \left[\frac{\kappa U_h}{\log(h/z_{0,\Delta})} \right]^2, \tag{4.9}$$

where $\langle \tau^{SGS}_{13,\Delta} \rangle$ is the surface stress induced by the SGS gravity waves. Solving (4.9) for $z_{0,\Delta}$ gives

$$\begin{aligned} z_{0,\Delta} &= h \exp\left\{ -\kappa U_h \left(-\langle \tau^{SGS}_{13,\Delta} \rangle + \frac{(\kappa U_h)^2}{\log^2(h/z_{0,s})} \right)^{-1/2} \right\} \\ &= h \exp\left[-\kappa U_h \left(u_*^2 \int_{-\pi/2}^{\pi/2} \int_{\pi/\Delta}^{k_c} k^2 \beta(k) S(k,\theta) \cos^2\theta \, \mathrm{d}k \, \mathrm{d}\theta + \frac{(\kappa U_h)^2}{\log^2(h/z_{0,s})} \right)^{-1/2} \right]. \end{aligned} \tag{4.10}$$

To evaluate the integration in the above equation, we use the data of LESns-R with high resolution. While the largest k in LESns-R does not reach k_c, the associated error is small because the wave energy density S reduces rapidly with increasing k. The effective SGS sea-surface wave amplitude σ_η^Δ is then calculated as

$$\sigma_\eta^\Delta = \sqrt{z_{0,\Delta}^2 - z_{0,s}^2} \Big/ \alpha_w. \tag{4.11}$$

The roughness index α_w should be constant if the σ_η^Δ model is physically realistic. Using the data from the fine-resolution LESns-R, the benchmark values for σ_η^Δ are obtained by (4.11). In the following analyses, the reference height in (4.10) is set to be at the 10th grid above the wave surface, $h = z_{10}$. This gives $h^+ = 57.8$ in wall units, so that the reference height falls within the logarithmic region of the boundary layer.

Figure 11 shows the dependence of σ_η^Δ on the filter wavenumber for cases CU6, CU10 and CU18. The benchmark values given by the LESns-R data and (4.11) are also plotted. In figure 11, σ_η^Δ is normalized by its value at the filter size of Δ_4. Therefore, the prescription of α_w value in (4.11) is not needed.

Previous studies (e.g. Makin *et al.* 1995; Janssen 2004) as well as the LESns-R results in § 4.1 have indicated that long waves are less effective in exerting form drag on wind than short waves. By putting equal weights on low and high wave

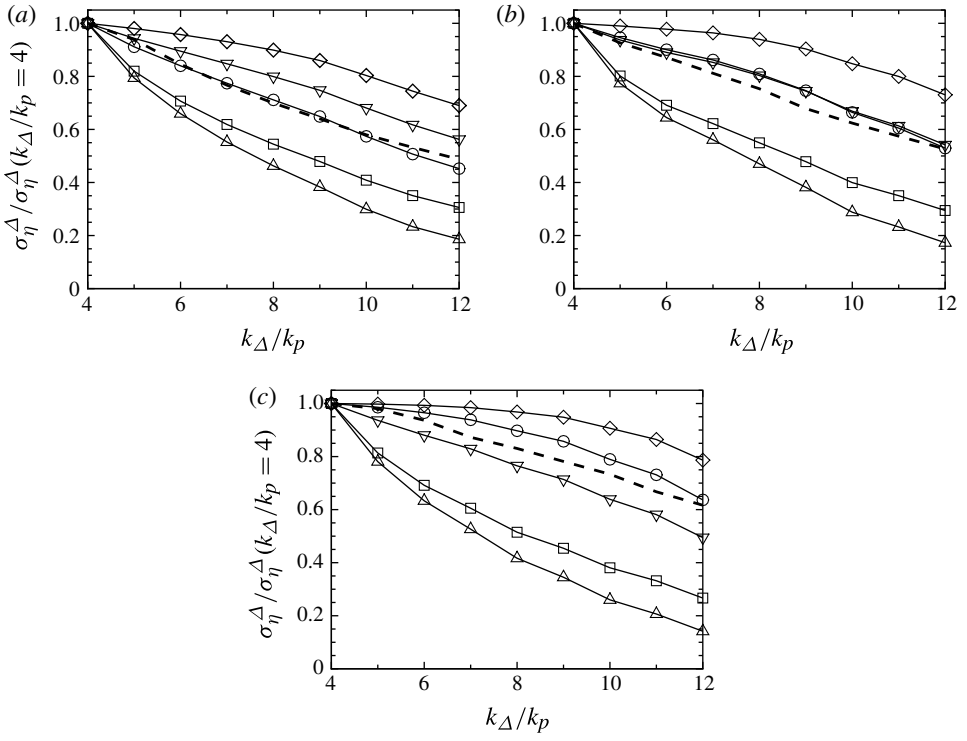

FIGURE 11. Dependence of the effective SGS wave amplitude σ_η^Δ on filter wavenumber k_Δ for various cases: (*a*) CU6; (*b*) CU10; and (*c*) CU18. Results of various roughness models are indicated by solid lines with symbols: ⊟, RMS model (equation (3.13)); ⧋, geometry model (equation (3.18)); ▽, steepness-dependent Charnock model (equation (3.21)); ⊖, wave-kinematics-dependent model (equation (3.25)); and ⟡, combined-kinematics-steepness model (equation (3.26)). Based on the LESns-R data, the benchmark value is calculated as $\sigma_\eta^\Delta = (z_{0,\Delta}^2 - z_{0,s}^2)^{1/2}/\alpha_w$ (equation (4.11)) with $z_{0,\Delta}$ given by (4.10). The benchmark is indicated by the dashed line. Normalization is done using the corresponding value of σ_η^Δ at $k_\Delta/k_p = 4$ for each model.

modes, the RMS model overestimates the decay of σ_η^Δ. The geometry model seems to put more weights on high wavenumbers by the multiplication with k in (3.18). However, the weights are insufficient and the calculation of σ_η^Δ in (3.18) does not involve a square-root operator as in other models. As a result, the geometry model also overestimates the decay of σ_η^Δ. The steepness-dependent Charnock model puts considerably more weights on high wavenumbers. However, the k^2 factor in (3.21) is relatively simple and can barely capture the wind–wave interaction physics accurately for all of the cases with different wave ages at the wave spectrum peak. As a result, the steepness-dependent Charnock model achieves good agreement with the benchmark data for case CU10, while overestimating σ_η^Δ for case CU6 and underestimating σ_η^Δ for case CU18. On the other hand, the combined-kinematics-steepness model underestimates the decay of σ_η^Δ with respect to k_Δ because the combination of the factor k^2 and the weighting function containing $\sqrt{g/k}$ in (3.26) is redundant. Finally, in the wave-kinematics-dependent model (equation (3.25)), the exponential weighting

Filter	RMS model	Geometry model	Steepness-dependent Charnock model	Wave-kinematics-dependent model	Combined-kinematics-steepness model
Δ_4	0.0869	0.633	3.80	0.325	16.52
Δ_5	0.0995	0.748	3.78	0.335	15.81
Δ_6	0.1040	0.811	3.59	0.328	14.58
Δ_7	0.1077	0.878	3.44	0.322	13.60
Δ_8	0.1116	0.956	3.32	0.320	12.85
Δ_9	0.1161	1.057	3.25	0.321	12.29
Δ_{10}	0.1233	1.226	3.24	0.329	11.91
Δ_{11}	0.1320	1.442	3.28	0.342	11.81
Δ_{12}	0.1385	1.657	3.29	0.351	11.67
σ_α^*	0.143	0.323	0.065	0.032	0.135

TABLE 3. Variations of the roughness index α_w with filter size for case CU6. The results are obtained using (4.9)–(4.11) and LESns-R data. The normalized standard deviation of α_w, σ_α^* (normalized by the mean value), is also shown.

Filter	RMS model	Geometry model	Steepness-dependent Charnock model	Wave-kinematics-dependent model	Combined-kinematics-steepness model
Δ_4	0.0533	0.463	6.572	0.455	58.45
Δ_5	0.0616	0.554	6.496	0.446	54.69
Δ_6	0.0672	0.625	6.433	0.440	52.09
Δ_7	0.0696	0.670	6.257	0.429	49.23
Δ_8	0.0731	0.741	6.163	0.424	46.86
Δ_9	0.0756	0.823	5.990	0.414	43.91
Δ_{10}	0.0833	1.003	6.132	0.428	43.02
Δ_{11}	0.0874	1.144	6.157	0.432	41.99
Δ_{12}	0.0953	1.409	6.383	0.452	42.11
σ_α^*	0.177	0.371	0.031	0.031	0.124

TABLE 4. Same as table 3, but for case CU10.

function reduces the weights on long waves, and significantly better agreement with the benchmark value is achieved compared with the other four models.

Tables 3–5 show the wave roughness index α_w for each model estimated using the LESns-R data. The value of α_w is obtained according to the following procedure. First, $z_{0,\Delta}$ is calculated by substituting the LESns-R data into (4.9) and (4.10). Meanwhile, the value of σ_η^Δ is obtained using the HOSM wave simulation data. Then the roughness index α_w is calculated according to (4.11). Note that the range of α_w values among different models differs significantly because of the different forms of σ_η^Δ for each model. In the tables, the normalized standard deviations (i.e. the r.m.s. value of variation normalized by the mean value) of α_w when changing the filter size are listed for each model. If a model is fully realistic, α_w should be fully independent of the filter size, and the normalized standard deviation of α_w should be zero.

Tables 3–5 indicate that the wave-kinematics-dependent model performs well, with the smallest value of the normalized standard deviation, for all of the three wave cases considered in the present study. The RMS model considers only the amplitude effect of surface waves, and thus behaves relatively well when the wave phase speed

Filter	RMS model	Geometry model	Steepness-dependent Charnock model	Wave-kinematics-dependent model	Combined-kinematics-steepness model
Δ_4	0.0162	0.189	6.653	0.650	243.2
Δ_5	0.0195	0.237	6.964	0.646	238.9
Δ_6	0.0220	0.279	7.077	0.630	229.4
Δ_7	0.0234	0.313	7.002	0.604	215.5
Δ_8	0.0262	0.376	7.222	0.601	208.6
Δ_9	0.0279	0.428	7.284	0.592	200.4
Δ_{10}	0.0312	0.532	7.636	0.604	196.7
Δ_{11}	0.0326	0.610	7.637	0.593	187.7
Δ_{12}	0.0375	0.823	8.294	0.630	190.7
σ_α^*	0.258	0.484	0.067	0.037	0.098

TABLE 5. Same as table 3 but for case CU18.

is small (case CU6) but performs poorly when the waves propagate fast (case CU18). The geometry model has the largest normalized standard deviation among all of the five models. As shown in figure 11, it differs the most compared with the benchmark data. The α_w value in the steepness-dependent Charnock model is less dependent on the filter size for case CU10, but has more variation for cases CU6 and CU18. In the combined-kinematics-steepness model, the α_w value is more dependent on filter size for case CU18 than for cases CU6 and CU10. This combined model is inferior to the wave-kinematics-dependent model and the steepness-dependent Charnock model alone, because of the aforementioned over-weighting in the spectral integration.

Overall, the *a priori* tests in this subsection indicate that among the five candidate expressions proposed in § 3.2, the wave-kinematics-dependent model provides the best performance in terms of modelled surface stress, SGS surface roughness and resolution independence.

4.3. *A posteriori tests of dynamic sea-surface roughness models*

In *a posteriori* tests, we perform surface modelled (LESns-M) simulations, with the SGS sea-surface roughness models implemented, at relatively low grid resolution ($48 \times 64 \times 64$) and compare the results with filtered data of LESns-R obtained at high grid resolution ($128 \times 256 \times 64$). Note that the vertical grid points are evenly distributed in the LESns-M, while they are finely clustered near the wave surface in the LESns-R. This gives grid size of $\Delta x^+ = 170.7$, $\Delta y^+ = 64.0$ and $\Delta z^+ = 64.0$ for the LESns-M. The resolution of the wavefield for HOSM remains at 128×256, the same as in LESns-R. This enables us to obtain accurate information about the SGS wavefield needed in the surface roughness modelling. The simulation time step is $\Delta t^+ = 0.3$. We consider the same wave cases as in the *a priori* tests (table 1).

The wave growth rates obtained by LESns-M with the wave-kinematics-dependent model are shown in figure 7. The agreement of the LESns-M results with the data in the literature and the results of the LESns-R runs is quite good, indicating that with a proper sea-surface roughness model, it is feasible to capture wind–wave interactions with LESns-M. Moreover, at low u_*/c, the values of γ for case CU18 obtained from LESns-M appear to be closer to the experimental results than those obtained from LESns-R are. Note that LESns-M uses the logarithmic law (equation (3.3)) on a computational grid coarser than that in LESns-R. This result further supports our surface-layer modelling approach.

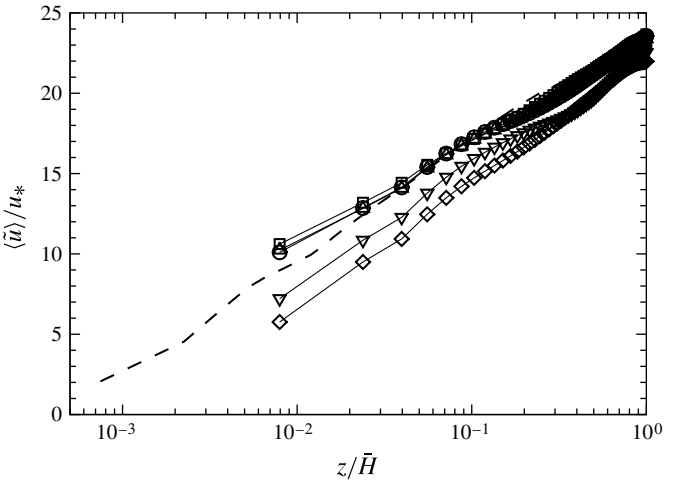

FIGURE 12. Normalized mean streamwise velocity profiles on a semi-logarithmic scale for case CU6. The result of LESns-R is indicated by − − −. The results from LESns-M with various sea-surface roughness models are indicated by solid lines with different symbols: ⊟, RMS model (equation (3.13)); ⧋, geometry model (equation (3.18)); ▽, steepness-dependent Charnock model (equation (3.21)); ⊖, wave-kinematics-dependent model (equation (3.25)); and ◇, combined-kinematics-steepness model (equation (3.26)).

Figures 12–18 show the mean vertical profiles of a variety of turbulence statistics. For the current cases with deformable wave surfaces, the mean value of a quantity is obtained by averaging over a plane of constant ζ and over time, where ζ is the vertical coordinate in the computational space as defined in § 2. Thus, the vertical coordinate in the physical space in figures 12–18 refers to the mean physical height of the grid points with the same ζ and approximately the same vertical distance to the wave surface.

Figure 12 shows the vertical profiles of mean streamwise velocity for case CU6. The results from LESns-M using the dynamic sea-surface roughness model are compared with the filtered result of LESns-R. Results from various models for σ_η^Δ discussed in § 3.2 are shown. It can be seen that the mean velocity profile from the LESns-M using the wave-kinematics-dependent model agrees best with the benchmark results obtained from the high-resolution LESns-R. The RMS model and the geometry model underestimate the sea-surface roughness, resulting in a slightly larger value for the streamwise velocity. On the other hand, both the steepness-dependent Charnock model and the combined-kinematics-steepness model overestimate the sea-surface roughness, which leads to reduced mean velocity. The performance of various roughness models shown here is consistent with the *a priori* test results in § 4.2.

Figure 13 shows the vertical profiles of shear stresses for case CU6 obtained by the LESns-M using the wave-kinematics-dependent model, which has been shown in preceding results to have the best performance among all five σ_η^Δ models and is thus the focus of the subsequent analyses. The mean total shear stress consists of three components, the resolved Reynolds stress $\langle\widetilde{u}'\widetilde{w}'\rangle$, the mean SGS shear stress $\langle\tau_{13}\rangle$ and the mean viscous shear stress $\nu_a\partial\langle\widetilde{u}\rangle/\partial z$. Here, the velocity fluctuations $\widetilde{u}_i'$ $(i = 1, 2, 3)$ are obtained by subtracting the corresponding plane- and time-averaged values from $\widetilde{u}_i$. The resolved Reynolds shear stress $\langle\widetilde{u}'\widetilde{w}'\rangle$ dominates and increases almost linearly

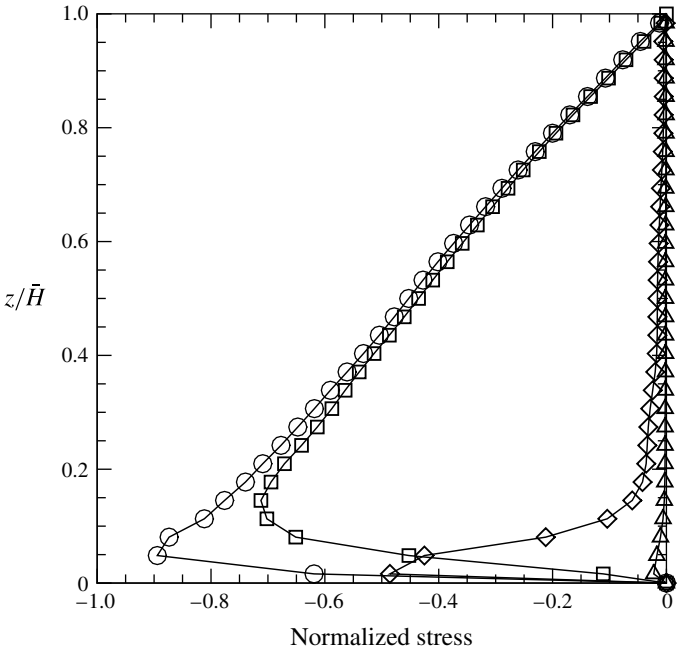

FIGURE 13. Vertical profiles of the shear stresses (normalized by u_*^2) for case CU6 obtained by the LESns-M with the sea-surface roughness being modelled by the wave-kinematics-dependent model: ⊟, the resolved Reynolds stress $\langle\widetilde{u}'\widetilde{w}'\rangle$; ⟡, the mean SGS shear stress $\langle\tau_{13}\rangle$; ⧋, the mean viscous shear stress $\nu_a\partial\langle\widetilde{u}\rangle/\partial z$; and ⊖, the total shear stress. Symbols are shown for every two grid points.

away from the top boundary until $z/\overline{H} = 0.1$ and then reduces rapidly towards the bottom wave boundary. The mean SGS shear stress $\langle\tau_{13}\rangle$ is small at elevated heights but increases rapidly towards the wave surface at $0.05 < z/\overline{H} < 0.1$; then its value decreases rapidly when further approaching the wave surface. The mean viscous shear stress $\nu_a\partial\langle\widetilde{u}\rangle/\partial z$ is negligible compared with the other two stress components. Similar to pressure-driven turbulent flow over a flat boundary, in the current case the total shear stress increases linearly as the distance from the top boundary increases. However, the total normalized shear stress does not reach -1 at the wave surface, because of the additional momentum loss associated with the resolved wave form drag (cf. Anderson & Meneveau 2010, 2011, for the static rough wall case).

Figure 14 shows the vertical profiles of velocity variances for case CU6. Results of LESns-M using dynamic sea-surface roughness models are compared with the filtered result of LESns-R. Similar to turbulence over static rough wall (Anderson & Meneveau 2010, 2011), for turbulence over water waves, the velocity variance is dominated by the streamwise component $\langle\widetilde{u}'\widetilde{u}'\rangle$, with the magnitude of the three components following the order of $\langle\widetilde{u}'\widetilde{u}'\rangle > \langle\widetilde{v}'\widetilde{v}'\rangle > \langle\widetilde{w}'\widetilde{w}'\rangle$. As shown in figure 14(*a,b*), the values of $\langle\widetilde{u}'\widetilde{u}'\rangle$ and $\langle\widetilde{v}'\widetilde{v}'\rangle$ obtained by LESns-M with the wave-kinematics-dependent model agree with the filtered result of LESns-R. The RMS model and geometry model also show consistent results but with slightly smaller magnitudes. The steepness-dependent Charnock model and combined-kinematics-steepness model apparently underestimate the horizontal velocity variances close to the wave surface. The difference among the results of different σ_η^Δ models is larger for the vertical

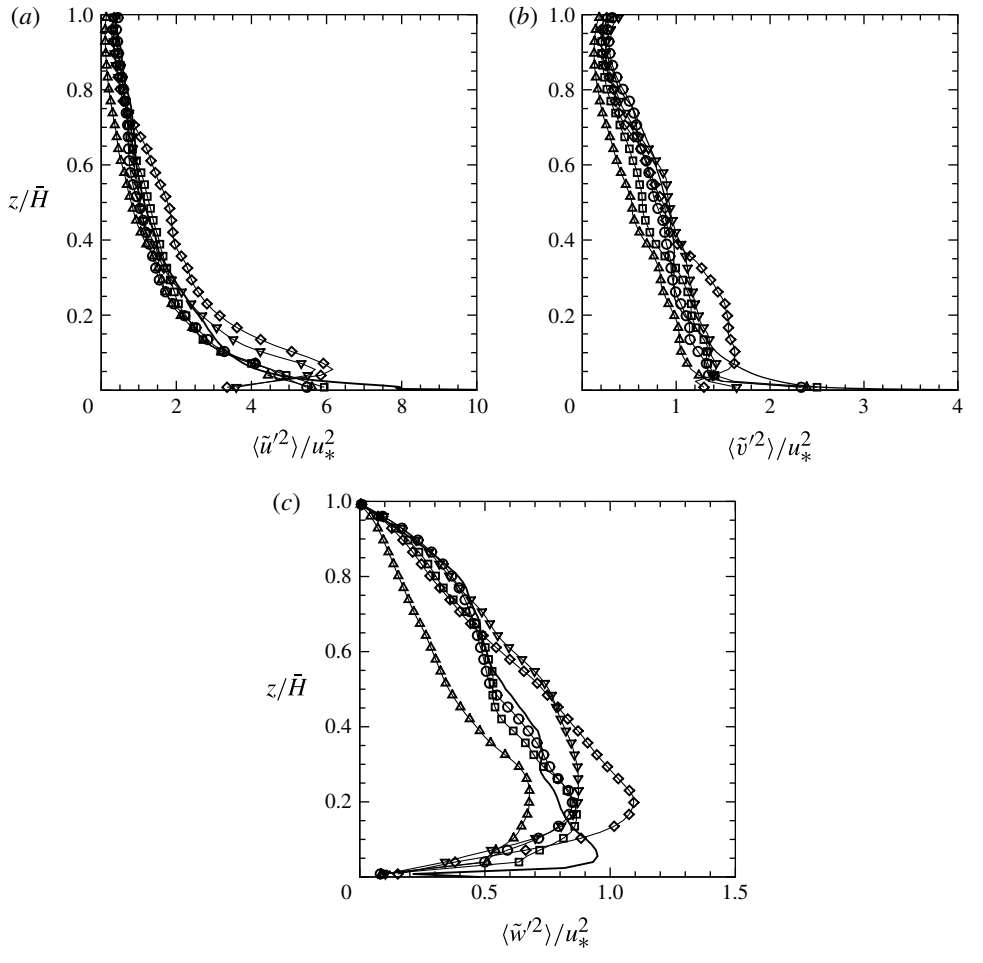

FIGURE 14. Vertical profiles of velocity variances for case CU6: (*a*) $\langle\widetilde{u}'^2\rangle$; (*b*) $\langle\widetilde{v}'^2\rangle$; and (*c*) $\langle\widetilde{w}'^2\rangle$. The filtered result of LESns-R is indicated by ——. Results from LESns-M with various sea-surface roughness models are indicated by solid lines with symbols: ⊟, RMS model (equation (3.13)); △, geometry model (equation (3.18)); ▽, steepness-dependent Charnock model (equation (3.21)); ⊖, wave-kinematics-dependent model (equation (3.25)); and ◇, combined-kinematics-steepness model (equation (3.26)). Symbols are shown for every two grid points.

velocity variance $\langle\widetilde{w}'\widetilde{w}'\rangle$ than that of the horizontal variances (figure 14*c*). The geometry model underestimates the magnitude of $\langle\widetilde{w}'\widetilde{w}'\rangle$, while the steepness-dependent Charnock model and combined-kinematics-steepness model overestimate the value. The filtered data of LESns-R agrees better with the results obtained by the RMS model and wave-kinematics-dependent model.

Figure 15 shows the vertical profiles of mean streamwise velocity for case CU10. Similar to case CU6, the RMS and geometry models overestimate the mean velocity in case CU10, but with even more appreciable deviations. The steepness-dependent Charnock model and combined-kinematics-steepness model underestimate the mean velocity for case CU10, as they did in case CU6. The wave-kinematics-dependent model still has the best performance among the five σ_η^Δ models. Figure 16 shows

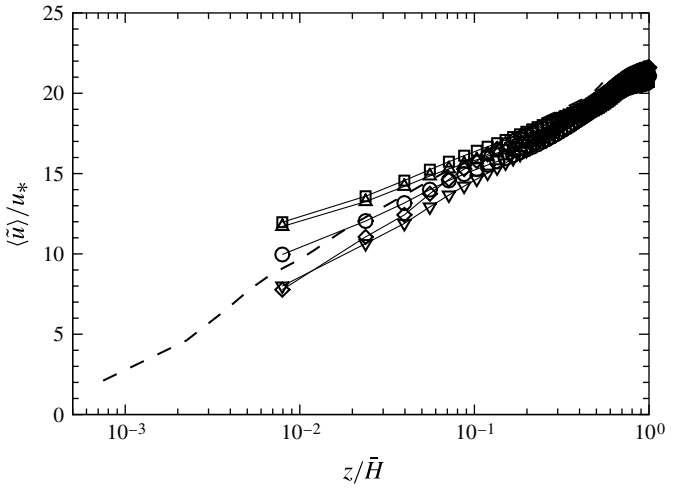

FIGURE 15. The same as in figure 12 but for case CU10.

the vertical profiles of velocity variances for case CU10. For the horizontal velocity variances (figure 16*a*,*b*), the results from LESns-M with various dynamic roughness models agree reasonably well with the benchmark results from LESns-R, except for the overestimation by the RMS model and the more appreciable overestimation by the combined-kinematics-steepness model. Except for the combined-kinematics-steepness model, all four other σ_η^Δ models capture the enhancement of the near-surface peak for $\langle\widetilde{u}'\widetilde{u}'\rangle$ due to the increase of wave phase speed when comparing case CU10 with case CU6 (cf. figure 14*a*). For the vertical velocity variance (figure 16*c*), results from the steepness-dependent Charnock model and wave-kinematics-dependent model agree with the benchmark results from LESns-R, with a slightly overestimated peak near the wave surface. But the RMS and geometry models obtain an appreciably larger peak near the wave surface. The combined-kinematics-steepness model overestimates the vertical velocity variance over all of the height.

For case CU18, the energy-containing waves in the wavefield propagate faster than those in cases CU6 and CU10, and the wave surface in CU18 is thus effectively smoother than those in cases CU6 and CU10 (also see Janssen 2004). The smaller total surface roughness for case CU18 is indicated by the larger value of mean streamwise velocity near the wave surface in figure 17 compared with figures 12 and 15. Furthermore, the difference between LESns-R and LESns-M with various σ_η^Δ models is also found to be less obvious compared with cases CU6 and CU10. The difference in the velocity variances is also small, as shown in figure 18. Compared with cases CU6 and CU10, in case CU18 the horizontal velocity variances have smaller magnitudes at high heights, but have a rapid increase in magnitude very close to the wave surface because of the strong velocity distortion by the fast propagating waves. Such strong wave distortion also results in a larger peak of $\langle\widetilde{w}'\widetilde{w}'\rangle$ adjacent to the wave surface as shown in figure 18(*c*), rather than a smaller peak somewhat above the wave surface for cases CU6 and CU10 as shown in figures 14(*a*) and 16(*a*), respectively.

In summary, the comparisons of the vertical profiles of mean streamwise velocity and velocity variances suggest that the current dynamic sea-surface roughness modelling approach works for LESns-M of turbulence over water waves. The results

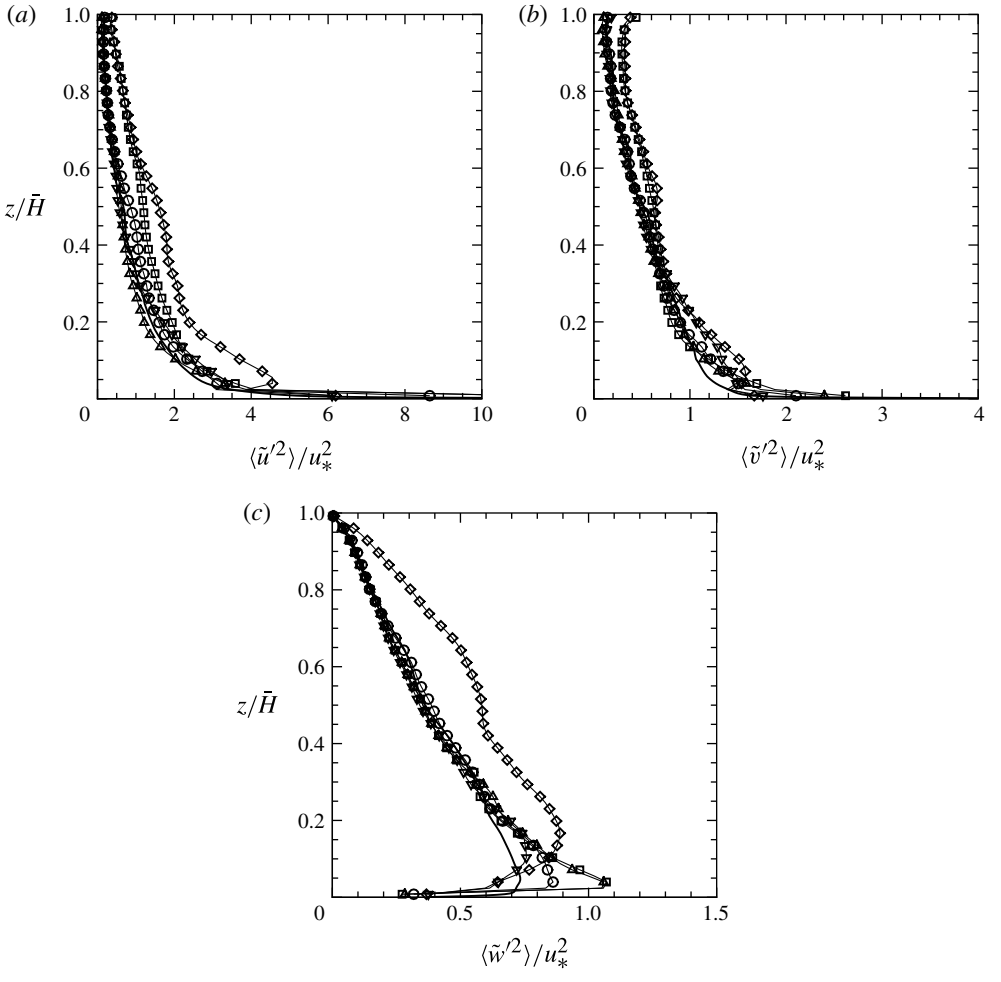

FIGURE 16. The same as in figure 14 but for case CU10.

of *a posteriori* tests shown in figures 12–18 together with the *a priori* test results in § 4.2 indicate consistently that the wave-kinematics-dependent model is the best among the five models for σ_η^Δ. Therefore, a dynamic sea-surface roughness model based on the wave kinematics (equations (3.7) and (3.25)) can be regarded as a method of choice for LESns-M of wind over waves.

5. Conclusions and discussion

In this study, a dynamic sea-surface roughness model has been developed for LES of wind turbulence over an ocean wavefield. In the simulations, the surface elevation and the corresponding air pressure variation of the waves are resolved down to GSs. As a result, the effects of GS waves on wind turbulence are captured through the wave-induced form drag on the wind turbulence. However, the effects of SGS waves are not resolved explicitly (in LESns-M) and are modelled using a local log-law surface model. In the log-law function, the roughness scale due to the SGS sea-surface waves is modelled by a coefficient α_w (in principle α_w is unknown), multiplied by an

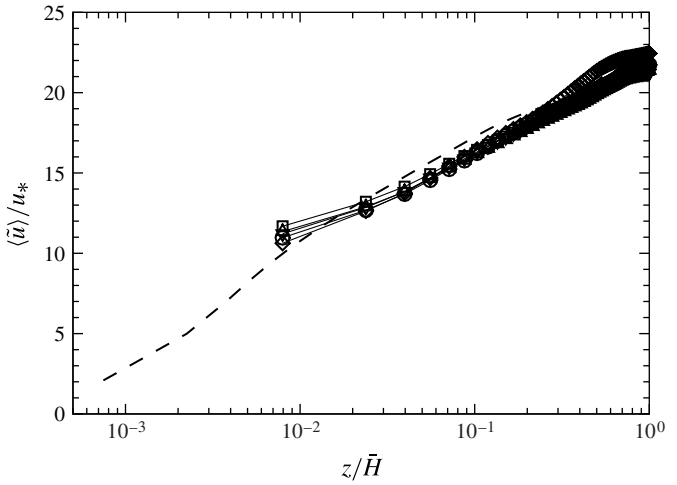

FIGURE 17. The same as in figure 12 but for case CU18.

effective SGS wave amplitude σ_η^Δ, which is quantified by a weighted integral over the SGS wave spectrum. In the present numerical framework, the wave simulation using HOSM employs higher resolution than the LES, in order to resolve a significant portion of the gravity waves within both the GS and SGS ranges. The value of σ_η^Δ is thus calculated directly by the numerical integration of the wave simulation result. The total surface stress is expressed as the sum of the GS form drag and the log-law-based SGS shear stress. Based on the physical constraint that the total surface stress is invariant with respect to the grid resolution, the total surface stresses at grid and test-filter scales are equated to form an equation for the unknown coefficient α_w. Such a dynamic approach allows the value of α_w to adjust to particular prevalent wind and wave conditions.

Five candidate models for σ_η^Δ based on different aspects of the wave characteristics are evaluated. They are named as the RMS model, geometry model, steepness-dependent Charnock model, wave-kinematics-dependent model and combined-kinematics-steepness model. They are tested for different wind–wave conditions. The performance of the models is evaluated by means of *a priori* tests using the benchmark data from high-resolution surface-resolving simulations (LESns-R), as well as *a posteriori* tests by implementing the approach in surface-modelled LES (LESns-M). Among the different models for σ_η^Δ, the wave-kinematics-dependent model yields the best performance consistently because it includes both the wave amplitude information (through the wave spectrum function) and the kinematics of wind-and-wave relative motion (through an exponential function that depends on the ratio of wave phase speed to wind friction velocity). Further assessment and analysis of the model performance based on the critical-layer theory is reported in Yang, Shen & Meneveau (2013), which shows results consistent with this paper.

In this study, we have focused on the development of a new sea-surface roughness model that is dynamic in LES. For future studies, a variety of modifications can be implemented to improve and generalize the current model. As the first attempt, we currently use only one unknown coefficient, α_w, in our dynamic roughness model and reasonably good results are obtained. The value of α_w is assumed to be scale-invariant. For future extension, one can use more than one dynamic parameter to take

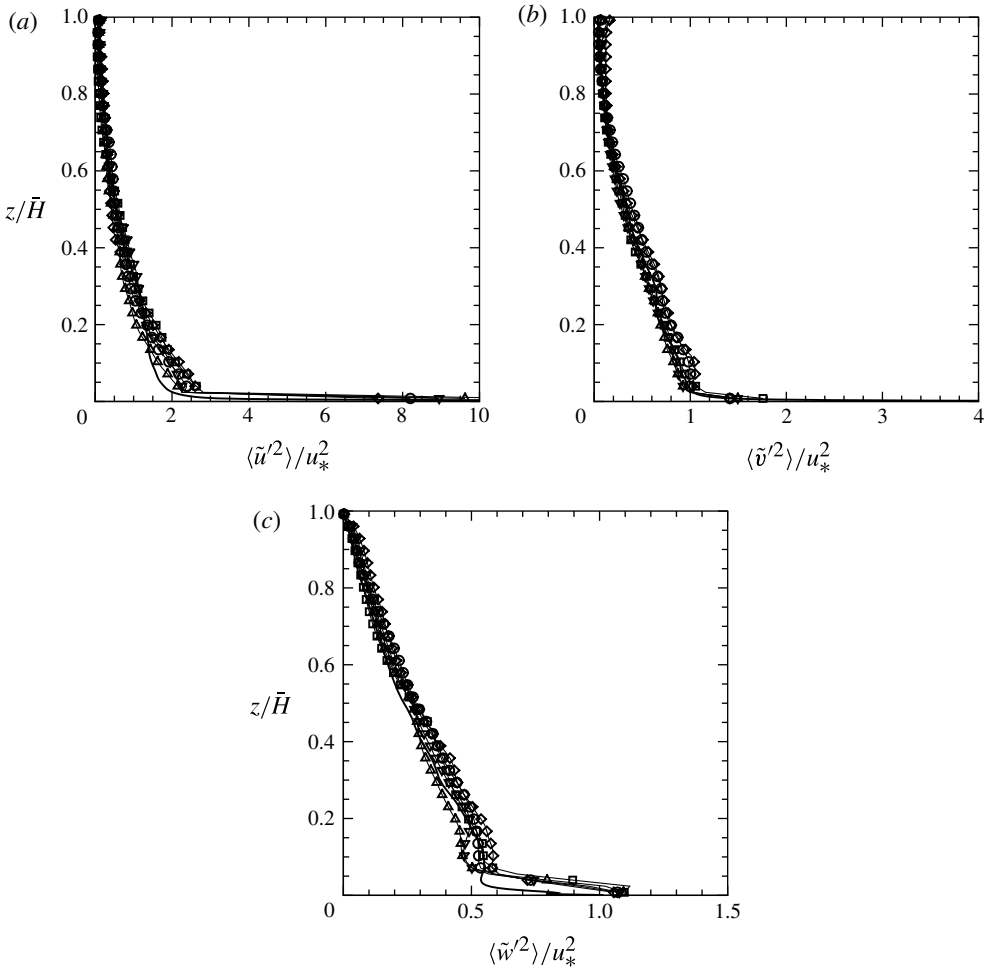

FIGURE 18. The same as in figure 14 but for case CU18.

into account the possible scale dependence of the model coefficient α_w. Moreover, the present study considers plane-averaging in the horizontal directions. In real applications, the sea-surface roughness varies spatially quite a bit. For example, the interaction among waves due to wave focusing may cause intermittent increases of wave steepness (e.g. Wu 2004). Another example is that a long wave may modulate the short waves riding on it and cause variations of surface roughness that are correlated with the phase of the long wave (e.g. Longuet-Higgins 1969; Gent & Taylor 1976). For these conditions, the current dynamic roughness model can be generalized using piecewise horizontal averaging or long-wave phase-averaging. Such extensions are straightforward in the framework established in this study, and will be investigated in our future research. Going forward, wave breaking effects could also be considered, although more in-depth studies are required to simulate and model breaking waves. Still, one can envision many further generalizations of the dynamic approach, based on first-principles constraints that should enforce that the same overall flux (e.g. of momentum or of various scalars) is predicted by the model, irrespective of grid resolution, thus providing additional equations for unknown model parameters.

Acknowledgements

D.Y. and L.S. acknowledge the support of the National Science Foundation (grants CBET-1133700 and OCE-1341063) and the Office of Naval Research (grant N00014-09-1-0395). C.M. acknowledges the support of the National Science Foundation (grant AGS-1045189). Conversations with Dr W. Anderson (now at Baylor University) are also gratefully acknowledged.

Appendix. Spectral description of wind-generated sea-surface waves

The frequency spectrum of the wave surface height obtained during the JONSWAP (Hasselmann *et al.* 1973) is expressed as

$$E_J(\omega) = \frac{\alpha_J g^2}{\omega^5} \exp\left[-\frac{5}{4}\left(\frac{\omega_p}{\omega}\right)^4\right] \gamma^r, \tag{A 1}$$

where

$$r = \exp\left[-\frac{(\omega-\omega_p)^2}{2\sigma^2\omega_p^2}\right], \tag{A 2}$$

$$\alpha_J = 0.076\left(\frac{U_{10}^2}{gF}\right)^{0.22}, \tag{A 3}$$

$$\omega_p = 22\left(\frac{g^2}{U_{10}F}\right)^{1/3}, \tag{A 4}$$

$$\gamma = 3.3, \tag{A 5}$$

$$\sigma = \begin{cases} 0.07 & \omega \leqslant \omega_p, \\ 0.09 & \omega > \omega_p. \end{cases} \tag{A 6}$$

Here, ω is the angular frequency, ω_p is the angular frequency at the spectrum peak, F, called the fetch, is the distance over which the wind has been blowing and γ is the peak enhancement factor. Based on the dispersion relation for deep-water waves, $\omega^2 = gk$, equation (A 1) is transformed into (3.8) in wavenumber space using

$$F_J(k) = \frac{g}{2\omega} E_J(\omega). \tag{A 7}$$

REFERENCES

ALBERTSON, J. D. & PARLANGE, M. B. 1999 Surface length scales and shear stress: implications for land–atmosphere interaction over complex terrain. *Water Resour. Res.* **35**, 2121–2132.

AL-ZANAIDI, M. A. & HUI, W. H. 1984 Turbulent airflow over water waves – a numerical study. *J. Fluid Mech.* **148**, 225–246.

ANDERSON, W. & MENEVEAU, C. 2010 A large-eddy simulation model for boundary-layer flow over surfaces with horizontally resolved but vertically unresolved roughness elements. *Boundary-Layer Meteorol.* **137**, 397–415.

ANDERSON, W. & MENEVEAU, C. 2011 Dynamic roughness model for large-eddy simulation of turbulent flow over multiscales, fractal-like rough surfaces. *J. Fluid Mech.* **679**, 288–314.

ANDERSON, W., PASSALACQUA, P., PORTÉ-AGEL, F. & MENEVEAU, C. 2012 Large-eddy simulation of atmospheric boundary-layer flow over fluvial-like landscapes using a dynamic roughness model. *Boundary-Layer Meteorol.* **144**, 263–286.

BELCHER, S. E. & HUNT, J. C. R. 1993 Turbulent shear flow over slowly moving waves. *J. Fluid Mech.* **251**, 109–148.

BELCHER, S. E. & HUNT, J. C. R. 1998 Turbulent flow over hills and waves. *Annu. Rev. Fluid Mech.* **30**, 507–538.

BOU-ZEID, E., MENEVEAU, C. & PARLANGE, M. 2005 A scale-dependent Lagrangian dynamic model for large eddy simulation of complex turbulent flows. *Phys. Fluids* **17**, 025105.

BOU-ZEID, E., PARLANGE, M. B. & MENEVEAU, C. 2006 On the parameterization of surface roughness at regional scales. *J. Atmos. Sci.* **64**, 216–227.

BYRNE, H. M. 1982 The variation of the drag coefficient in the marine surface layer due to temporal and spatial variations in the wind sea state. PhD thesis, University of Washington.

CALHOUN, R. J., STREET, R. J. & KOSEFF, J. R. 2001 Turbulent flow over a wavy surface: stratified case. *J. Geophys. Res.* **106**, 9295–9310.

CARTWRIGHT, D. E. 1963 The use of directional spectra in studying the output of a wave recorder on a moving ship. In *Ocean Wave Spectra*, pp. 203–218. Prentice Hall.

CAUDAL, G. 1993 Self-consistency between wind stress, wave spectrum, and wind-induced wave growth for fully rough air–sea interface. *J. Geophys. Res.* **98**, 22743–22752.

CAVALERI, L., ALVES, J.-H. G. M., ARDHUIN, F., BABANIN, A., BANNER, M., BELIBASSAKIS, K., BENOIT, M., DONELAN, M., GROENEWEG, J., HERBERS, T. H. C., HWANG, P., JASSEN, P. A. E. M., JASSEN, T., LAVRENOV, I. V., MAGNE, R., MONBALIU, J., ONORATO, M., POLNIKOV, V., RESIO, D., ROGERS, W. E., SHEREMET, A., SMITH, J. M., TOLMAN, H. L., VAN VLEDDER, G., WOLF, J. & YOUNG, I. 2007 Wave modelling – the state of the art. *Prog. Oceanogr.* **75**, 603–674.

CHARNOCK, H. 1955 Wind stress on a water surface. *Q. J. R. Meteorol. Soc.* **81**, 639–640.

COHEN, J. E. & BELCHER, S. E. 1999 Turbulent shear flow over fast-moving waves. *J. Fluid Mech.* **386**, 345–371.

DEARDORFF, J. W. 1973 The use of subgrid transport equations in a three-dimensional model of atmospheric turbulence. *Trans. ASME: J. Fluids Engng* **95**, 429–438.

DOBSON, F. W. 1971 Measurements of atmospheric pressure on wind-generated sea waves. *J. Fluid Mech.* **48**, 91–127.

DOMMERMUTH, D. G. & YUE, D. K. P. 1987 A high-order spectral method for the study of nonlinear gravity waves. *J. Fluid Mech.* **184**, 267–288.

DONELAN, M. A. 1990 Air–sea interaction. In *The sea* (ed. B. LeMehaute & D. M. Hanes), vol. 9, pp. 239–292. Wiley-Interscience.

DONELAN, M. A. 1999 Wind-induced growth and attenuation of laboratory waves. In *Wind-over-Wave Couplings: Perspectives and Prospects* (ed. S. G. Aajjadi, N. H. Thomas & J. C. R. Hunt), pp. 183–194. Clarendon.

DONELAN, M. A., BABANIN, A. V., YOUNG, I. R. & BANNER, M. L. 2006 Wave-follower field measurements of the wind-input spectral function. Part II. Parameterization of the wind input. *J. Phys. Oceanogr.* **36**, 1672–1689.

DRENNAN, W. M., TAYLOR, P. K. & YELLAND, M. J. 2005 Parameterizing the sea surface roughness. *J. Phys. Oceanogr.* **35**, 835–848.

VAN DUIN, C. A. & JANSSEN, P. A. E. M. 1992 A numerical model of the air flow above water waves. *J. Fluid Mech.* **236**, 197–215.

ELLIOTT, J. A. 1972 Microscale pressure fluctuations near waves being generated by the wind. *J. Fluid Mech.* **54**, 427–448.

FAIRALL, C. W., BRADLEY, E. F., ROGERS, D. P., EDSON, J. B. & YOUNG, G. S. 1996 Bulk parameterization of air–sea fluxes for tropical ocean-glocal atmosphere coupled-ocean atmosphere response experiment. *J. Geophys. Res.* **101**, 3747–3764.

GEERNAERT, G. L. 1983 Variation of the drag coefficient and its dependence on sea state. PhD thesis, University of Washington.

GENT, P. R. & TAYLOR, P. A. 1976 A numerical model of the air flow above water waves. *J. Fluid Mech.* **77**, 105–128.

GERMANO, M., PIOMELLI, U., MOIN, P. & CABOT, W. H. 1991 A dynamic subgrid-scale eddy viscosity model. *Phys. Fluids* A **3**, 1760–1770.

HASSELMANN, K., BARNETT, T. P., BOUWS, E., CARLSON, H., CARTWRIGHT, D. E., ENKE, K., EWING, J. A., GIENAPP, H., HASSELMANN, D. E., KRUSEMAN, P., MEERBURG, A., MÜLLER, P., OLBERS, D. J., RICHTER, K., SELL, W. & WALDEN, H. 1973 Measurements of wind–wave growth and swell decay during the Joint North Sea Wave Project (JONSWAP). *Dtsch. Hydrogr. Z. Suppl.* **8** (12), 1–95.

HASSELMANN, D. E., DUNCKEL, M. & EWING, J. A. 1980 Directional wave spectra observed during JONSWAP 1973. *J. Phys. Oceanogr.* **10**, 1264–1280.

HENN, D. S. & SYKES, R. I. 1999 Large-eddy simulation of flow over wavy surfaces. *J. Fluid Mech.* **383**, 75–112.

HRISTOV, T. S., MILLER, S. D. & FRIEHE, C. A. 2003 Dynamical coupling of wind and ocean waves through wave-induced air flow. *Nature* **422**, 55–58.

HSU, S. A. 1974 A dynamic roughness equation and its application to wind stress determination at the air–sea interface. *J. Phys. Oceanogr.* **4**, 116–120.

JANSSEN, P. A. E. M. 1991 Quasi-linear theory of wind–wave generation applied to wave forecasting. *J. Phys. Oceanogr.* **21**, 1631–1642.

JANSSEN, P. 2004 *The Interaction of Ocean Waves and Wind*. Cambridge University Press.

JOHNSON, H. K., HØSTRUP, J., VESTED, H. J. & LARSEN, S. E. 1998 On the dependence of sea surface roughness on wind waves. *J. Phys. Oceanogr.* **28**, 1702–1716.

KIHARA, N., HANAZAKI, H., MIZUYA, T. & UEDA, H. 2007 Relationship between airflow at the critical height and momentum transfer to the traveling waves. *Phys. Fluids* **19**, 015102.

KINCAID, D. & CHENEY, W. 2001 *Numerical Analysis: Mathematics of Scientific Computing*, 3rd edn. Brooks Cole.

KITAIGORODSKII, S. A. 1968 On the calculation of the aerodynamic roughness of the sea surface. *Izv. Atmos. Ocean. Phys.* **4**, 870–878.

KITAIGORODSKII, S. A. & VOLKOV, Y. A. 1965 On the roughness parameter of the sea surface and the calculation of momentum flux in the near water layer of the atmosphere. *Bull. Acad. Sci. USSR Atmos. Ocean. Phys.* **1**, 973–988.

KUMAR, V., SVENSSON, G., HOLTSLAG, A. A. M., MENEVEAU, C. & PARLANGE, M. B. 2010 Impact of surface flux formulations and geostrophic forcing on large-eddy simulations of diurnal atmospheric boundary layer flow. *J. Appl. Meteor. Climat.* **49**, 1496–1516.

LAMB, H. 1932 *Hydrodynamics*. Dover.

LETTAU, H. 1969 Note on aerodynamic roughness-parameter estimation on the basis of roughness-element description. *J. Appl. Meteorol.* **8**, 828–832.

LILLY, D. K. 1992 A proposed modification of the Germano subgrid-scale closure method. *Phys. Fluids* A **4**, 633–635.

LIU, Y., YANG, D., GUO, X. & SHEN, L. 2010 Numerical study of pressure forcing of wind on dynamically evolving water waves. *Phys. Fluids* **22**, 041704.

LONGUET-HIGGINS, M. S. 1969 A nonlinear mechanism for the generation of sea waves. *Proc. R. Soc. Lond.* A **331**, 371–389.

MAKIN, V. K., KUDRYAVTSEV, V. N. & MASTENBROEK, C. 1995 Drag of the sea surface. *Boundary-Layer Meteorol.* **73**, 159–182.

MASTENBROEK, C., MAKIN, V. K., GARAT, M. H. & GIOVANANGELI, J. P. 1996 Experimental evidence of the rapid distortion of turbulence in the air flow over water waves. *J. Fluid Mech.* **318**, 273–302.

MEI, C. C., STIASSNIE, M. & YUE, D. K. P. 2005 *Theory and Applications of Ocean Surface Waves. Part 2: Nonlinear Aspects*. World Scientific.

MILES, J. W. 1957 On the generation of surface waves by shear flows. *J. Fluid Mech.* **3**, 185–204.

MILES, J. W. 1993 Surface-wave generation revisited. *J. Fluid Mech.* **256**, 427–441.

MOENG, H. 1984 A large-eddy simulation for the study of planetary boundary layer turbulence. *J. Atmos. Sci.* **41**, 2052–2062.

PEIRSON, W. & GARCIA, A. W. 2008 On the wind-induced growth of slow water waves of finite steepness. *J. Fluid Mech.* **608**, 243–274.

PHILLIPS, O. M. 1957 On the generation of waves by turbulent wind. *J. Fluid Mech.* **2**, 417–445.

PIOMELLI, U. & BALARAS, E. 2002 Wall-layer models for large-eddy simulations. *Annu. Rev. Fluid Mech.* **34**, 349–374.

PLANT, W. J. 1982 A relationship between wind stress and wave slope. *J. Geophys. Res.* **87**, 1961–1967.

POPE, S. B. 2000 *Turbulent Flows*. Cambridge University Press.

PORTÉ-AGEL, F., MENEVEAU, C. & PARLANGE, M. B. 2000 A scale-dependent dynamic model for large-eddy simulation: application to a neutral atmospheric boundary layer. *J. Fluid Mech.* **415**, 261–284.

SMITH, S. D. 1988 Coefficients for sea surface wind stress, heat flux and wind profiles as a function of wind speed and temperature. *J. Geophys. Res.* **93**, 15467–15472.

SMITH, S. D., ANDERSON, R. J., OOST, W. A., KRAAN, C., MAAT, N., DECOSMO, J., KATSAROS, K. B., DAVIDSON, K. L., BUMKE, K., HASSE, L. & CHADWICK, H. M. 1992 Sea surface wind stress and drag coefficients: the HEXOS results. *Boundary-Layer Meteorol.* **60**, 109–142.

SNYDER, R. L., DOBSON, F. W., ELLIOTT, J. A. & LONG, R. B. 1981 Array measurements of atmospheric pressure fluctuations above surface gravity waves. *J. Fluid Mech.* **102**, 1–59.

SULLIVAN, P. P., EDSON, J. B., HRISTOV, T. & MCWILLIAMS, J. C. 2008 Large-eddy simulations and observations of atmospheric marine boundary layers above nonequilibrium surface waves. *J. Atmos. Sci.* **65**, 1225–1245.

SULLIVAN, P. P. & MCWILLIAMS, J. C. 2010 Dynamics of winds and currents coupled to surface waves. *Annu. Rev. Fluid Mech.* **42**, 19–42.

SULLIVAN, P. P., MCWILLIAMS, J. C. & HRISTOV, T. 2010 A large eddy simulation model of high wind marine boundary layers above a spectrum of resolved moving waves. In *19th Conference on Boundary Layer and Turbulence, Keystone, CO*.

SULLIVAN, P. P., MCWILLIAMS, J. C. & MOENG, C.-H. 2000 Simulation of turbulent flow over idealized water waves. *J. Fluid Mech.* **404**, 47–85.

TAYLOR, P. K. & YELLAND, M. J. 2001 The dependence of sea surface roughness on the height and steepness of the waves. *J. Phys. Oceanogr.* **31**, 572–590.

TOBA, Y., SMITH, S. D. & EBUCHI, N. 2001 Historical drag expressions. In *Wind Stress over the Ocean* (ed. I. S. F. Jones & Y. Toba), pp. 35–53. Cambridge University Press.

TOWNSEND, A. A. 1972 Flow in a deep turbulent boundary layer over a surface distorted by water waves. *J. Fluid Mech.* **55**, 719–735.

WEST, B. J., BRUECKNER, K. A. & JANDA, P. S. 1987 A new numerical method for surface hydrodynamics. *J. Geophys. Res.* **92**, 11803–11824.

WU, G. 2004 Direct simulation and deterministic prediction of large-scale nonlinear ocean wave-field. PhD thesis, Massachusetts Institute of Technology.

YANG, D. & SHEN, L. 2009 Characteristics of coherent vortical structures in turbulent flows over progressive surface waves. *Phys. Fluids* **21**, 125106.

YANG, D. & SHEN, L. 2010 Direct-simulation-based study of turbulent flow over various waving boundaries. *J. Fluid Mech.* **650**, 131–180.

YANG, D. & SHEN, L. 2011*a* Simulation of viscous flows with undulatory boundaries. Part I. Basic solver. *J. Comput. Phys.* **230**, 5488–5509.

YANG, D. & SHEN, L. 2011*b* Simulation of viscous flows with undulatory boundaries. Part II. Coupling with other solvers for two-fluid computations. *J. Comput. Phys.* **230**, 5510–5531.

YANG, D., SHEN, L. & MENEVEAU, C. 2013 An assessment of dynamic subgrid-scale sea-surface roughness models. *Flow Turbul. Combust.* doi:10.1007/s10494-013-9459-7.

ZAKHAROV, V. E. 1968 Stability of periodic waves of finite amplitude on the surface of a deep fluid. *J. Appl. Mech. Tech. Phys.* **9**, 190–194.